

Star Formation Sites toward the Galactic Center Region

The Correlation of CH₃OH Masers, H₂O Masers, and Near-IR Green Sources

E. T. Chambers¹, F. Yusef-Zadeh², and J. Ott³

¹ I. Physikalisches Institut, Universität zu Köln, Zùlpicher Str. 77, 50937 Köln, Germany
e-mail: chambers@ph1.uni-koeln.de

² Department of Physics and Astronomy and Center for Interdisciplinary Research in Astronomy, Northwestern University, Evanston, IL 60208

³ National Radio Astronomy Observatory, 1003 Lopezville Road, Socorro, NM 87801

Received xxxx; accepted xxxx

ABSTRACT

Aims. We present a study of star formation in the Central Molecular Zone (CMZ) of our Galaxy through the association of three star formation indicators: 6.7 GHz CH₃OH masers, 22 GHz H₂O masers, and enhanced 4.5 μ m emission (‘green’) sources. We explore how star formation in the Galactic center ($|\ell| < 1.3^\circ$, $|b| < 10'$, where ℓ and b are Galactic longitude and Galactic latitude) compares with that of the Galactic disk ($6^\circ < \ell < 345^\circ$, $|b| < 2^\circ$).

Methods. Using an automated algorithm, we search for enhanced 4.5 μ m emission sources toward 6.7 GHz CH₃OH masers detected in the Parkes Methanol Multibeam Survey. We combine these results with our 22 GHz H₂O maser survey of the CMZ carried out with the Mopra telescope.

Results. We find that the correlation of CH₃OH masers with green sources is a function of Galactic latitude, with a minimum close to $b=0$ and increasing with $|b|$ (toward the central part of the Galaxy, $6^\circ < \ell < 345^\circ$, $|b| < 2^\circ$). We find no significant difference between the correlation rate of CH₃OH masers with green sources in the CMZ and the disk. This suggests that although the physical conditions of the gas are different in the Galactic center from that of the Galactic disk, once gravitational instability sets in at sufficiently high densities, signatures of star formation appear to be similar in both regions. Moreover, the detection of green sources, even at the distance of the Galactic center, shows that our technique can easily identify the early stages of star formation, especially in low extinction regions of the Galaxy. Through the association of H₂O and CH₃OH masers, we identify 15 star-forming sites in the CMZ. We find no coincident H₂O and CH₃OH masers outside the CMZ (with limited H₂O maser survey coverage outside the CMZ), possibly indicating a difference in the maser evolutionary sequence for star-forming cores in the Galactic center region and the disk.

Key words. ISM: clouds–ISM: molecules–stars: formation–Galaxy: center

1. Introduction

As the nearest galactic nucleus, our Galactic center (GC) provides us with the opportunity to study in detail the star formation process in the extreme conditions at the centers of galaxies. The inner few hundred pc of the Galactic center, known as the Central Molecular Zone (CMZ) contains few times $10^7 M_\odot$ of molecular gas (Pierce-Price et al. 2000; Ferrière et al. 2007; Longmore et al. 2012) and hosts several prominent sites of star formation regions (e.g., Sgr A, Sgr B2 and Sgr C; see Fig. 1). By studying sites of star formation in this complex region, we can learn global characteristics of star formation process and compare with nuclei of other galaxies.

The CMZ is characterized to be different from the Galactic disk in several ways, such as its chemistry (Martín-Pintado et al. 2000; Oka et al. 2005; Riquelme et al. 2010; Jones et al. 2011, 2012, 2013; Yusef-Zadeh et al. 2013a), a two-temperature distribution of molecular gas (e.g., Hüttemeister et al. 1998; Mills & Morris 2013), its dust temperature being lower than its gas temperature (Odenwald & Fazio 1984; Cox & Laureijs 1989; Pierce-Price et al. 2000; Ferrière et al. 2007; Molinari et al. 2011; Immer et al. 2012), stronger turbulence (cf. Morris & Serabyn 1996), and evidence that it is a

region dominated by cosmic rays (Yusef-Zadeh et al. 2013a,b; Ao et al. 2013). Using thermal dust emission data from the *Herschel* Hi-GAL Key-Project, Molinari et al. (2011) have shown that much of this mass ($\sim 3 \times 10^7 M_\odot$) resides in a filamentary, twisted ring-like structure that encircles the center of the Galaxy. This ring has a projected extent of ~ 180 pc, is comprised of a dense, cold ($T \leq 20$ K) dust cloud with high column density that encloses warmer dust ($T \geq 25$ K) with lower column density in the interior of the ring. The recent results of Jones et al. (2012), who used the Mopra telescope to map the CMZ in ~ 20 molecular transitions at ~ 3 mm, show that the clouds in the region display bright emission with large linewidths and profiles consisting of several velocity components, all indicating the complex kinematic structure and composition of the gas in the Galactic center zone.

While it is clear that physical characteristics of the gas are unique in the CMZ, it is not clear how star formation in this region compares to that of the Galactic disk. Assuming that the gas is distributed uniformly throughout the inner 400 pc of the Galaxy rather than in a ring geometry, the Kennicutt law (Kennicutt 1998) still holds in a region where tidal shear could be important (Yusef-Zadeh et al. 2009). To make the comparison between star formation in the CMZ and in the Galactic disk, we

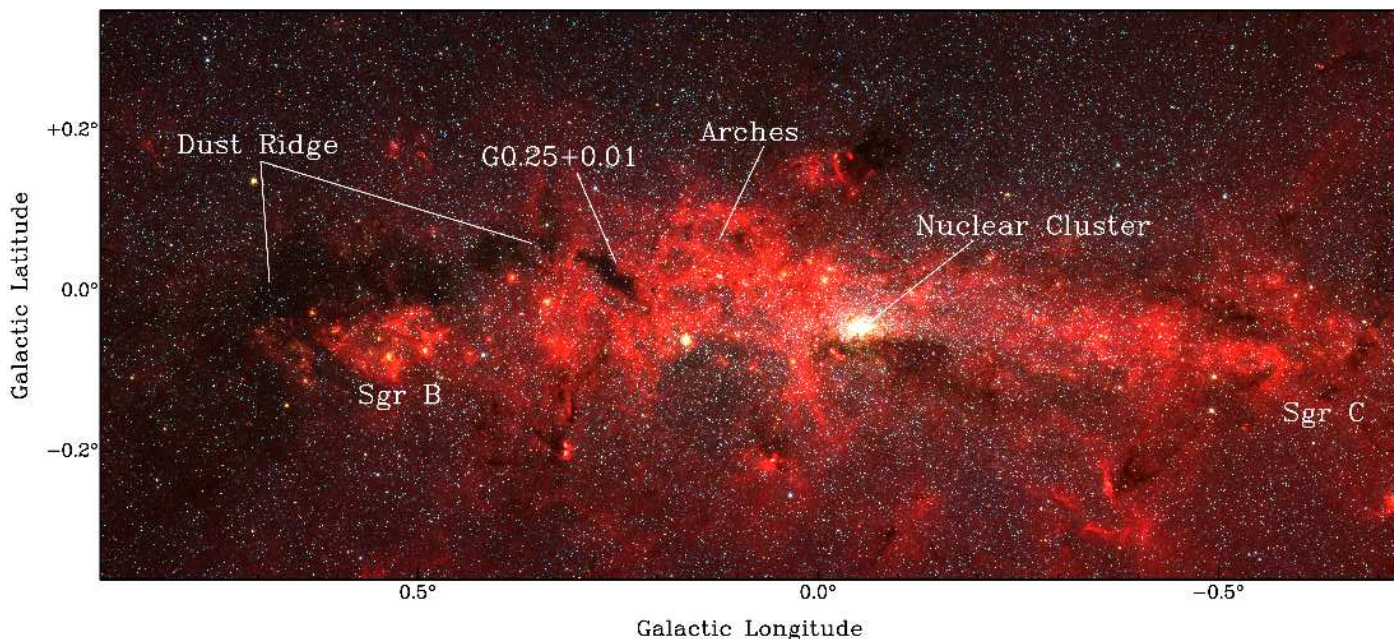


Fig. 1. *Spitzer*/IRAC 3-color image (with $8.0\ \mu\text{m}$ in red, $4.5\ \mu\text{m}$ in green, and $3.6\ \mu\text{m}$ in blue) of the Central Molecular Zone. Some of the more prominent Galactic center features are labelled. Sgr A* is centered on the nuclear cluster.

look at the correlation of two star formation indicators—maser emission (from both CH_3OH and H_2O) and extended, enhanced $4.5\ \mu\text{m}$ emission. Because of their different emission mechanisms, the correlation between the two can help constrain the evolutionary states of protostars.

The Class II CH_3OH maser transition at 6.7 GHz is one of the brightest known maser lines and is known to be an excellent signpost of star formation (e.g., Menten 1991; Minier et al. 2003; Caswell et al. 2010). The population inversion that gives rise to the transition is thought to be radiatively pumped, presumably by a central high-mass ($\geq 8\ M_\odot$) protostellar object (Cragg et al. 1992). It has been shown that this maser traces only high-mass star formation (Walsh et al. 2001; Minier et al. 2003), and is typically found close to protostars (Caswell 1997; Ellingsen 2005). As such, it is used as a marker of high-mass star formation throughout the Galaxy. Another well-known signpost of star formation is the H_2O maser transition at 22.23 GHz (Genzel et al. 1978; Gwinn 1994; Claussen et al. 1998; Furuya et al. 2001). The population inversion is created in shocks and outflows (Norman & Silk 1979; Elitzur et al. 1989; Hollenbach et al. 2013), and the maser is associated with both low- and high-mass star formation (as well as AGB stars and super-massive black holes), and has been the target of many recent observations and surveys (e.g., Caswell et al. 2011; Walsh et al. 2011). Many young star forming sites in the Galaxy harbor both CH_3OH and H_2O masers.

A more recently discovered tracer of star formation activity is extended, enhanced $4.5\ \mu\text{m}$ emission, commonly known as ‘green fuzzies’ (Chambers et al. 2009) or extended green objects (EGOs; Cyganowski et al. 2008). These sources appear green in *Spitzer*/IRAC (Fazio et al. 2004) 3-color images ($8.0\ \mu\text{m}$ in red, $4.5\ \mu\text{m}$ in green, and $3.6\ \mu\text{m}$ in blue). The $4.5\ \mu\text{m}$ enhancement is likely due to a shock-excited H_2 feature in the $4.5\ \mu\text{m}$ band (Noriega-Crespo et al. 2004; De Buizer & Vacca 2010; Foster et al. 2011), but it could also be from a shocked CO feature (Marston et al. 2004). While its exact nature is still uncertain, this $4.5\ \mu\text{m}$ emission, frequently referred to as ‘green’ emission throughout this paper, is a reliable tracer

of the early stages of star formation (Chambers et al. 2009; Cyganowski et al. 2008, 2009).

There have been several studies that show the correlation of green sources with maser emission. Yusef-Zadeh et al. (2007) found an association of green sources with 6.7 GHz CH_3OH masers toward the Galactic center, and other studies have since found similar correlations in the Galactic disk, with both 6.7 GHz CH_3OH and 22 GHz H_2O masers (Chambers et al. 2009; Chen et al. 2009; Cyganowski et al. 2009). Using a sample of 31 green sources (15 in the CMZ, and 16 foreground to the Galactic center region), Chambers et al. (2011) searched for a difference in the correlation rate of 6.7 GHz CH_3OH masers with green sources between the CMZ and the Galactic disk. They found no significant difference in the correlation rate, but that study suffered from small-number statistics.

In this paper, we search for differences in the correlation of masers with green sources between the Galactic center and the Galactic disk using a different approach. While the studies mentioned above search for maser emission toward samples of green sources, we instead search for extended, enhanced $4.5\ \mu\text{m}$ emission toward 6.7 GHz CH_3OH maser emission. We then correlate the results with a list of H_2O masers identified in a 22.23 GHz Mopra H_2O maser survey of the CMZ. This method has several advantages, such as a large sample of CH_3OH masers from the Parkes Methanol Multibeam Survey (Caswell et al. 2010). Moreover, it uses an automated, uniform approach to identifying enhanced $4.5\ \mu\text{m}$ emission. Finally, it makes use of H_2O masers as a third tracer of star formation indicator. Using this method, we explore how star formation in the Galactic center compares with that of the Galactic disk and identify sites of star formation using three different tracers.

The structure of this paper is as follows. In Section 2, we present our Mopra H_2O maser survey of the Galactic center region, along with brief descriptions of the CH_3OH maser survey carried out by Caswell et al. (2010) and the *Spitzer*/IRAC survey of the GC region. We describe our source detection and correlation algorithms in Section 3. In Sections 4 and 4.2, we present the results of applying the methods in Section 3 to the data in

Section 2. We discuss these results in Section 5, and summarize our findings in Section 6.

2. Data

2.1. 6.7 GHz CH₃OH Masers

The 6.7 GHz CH₃OH masers we use in our analysis were identified by Caswell et al. (2010, C10 hereafter) as part of the Parkes Methanol Multibeam Survey. Initial detections of the 6.7 GHz CH₃OH masers were made with the Parkes Observatory ¹, and subsequent follow-up observations with the Australia Telescope Compact Array to pinpoint the maser locations to 0.4'' accuracy. The full survey covers the entire Galactic plane with a latitude range of $|b| < 2^\circ$. C10 published a subset of this survey, covering $6^\circ < \ell < 345^\circ$, $|b| < 2^\circ$ with a 1σ detection limit of 0.07 Jy.

2.2. H₂O Maser Data

We observed the Galactic center region with the CSIRO/CASS Mopra² telescope in the period 2006 Sep 13 to 2006 Oct 15 and 2007 July 24 to September 17. Data were taken in the on-the-fly mode, dumping data every 2 s with the then newly installed 12mm receiver, dual polarization. We observed the Galactic longitude range of $-1.5^\circ < \ell < 2^\circ$ and Galactic latitude range of $|b| < 0.5^\circ$. The entire area was split into smaller, typically 18' on-the-fly subfields that were repeatedly and alternately observed in Galactic latitude and longitude directions, at least four times.

As a reference position we observed at $(\ell, b) = (4.301^\circ, 1.667^\circ)$ after every row. The data were calibrated with an internal noise diode. At the time of the observations in 2006, however, the noise diode was not fully calibrated itself and we used the 2007 observations to obtain pointed observations in each on-the-fly field from which we re-calibrated the 2006 data. The absolute calibration is estimated to be accurate to $\sim 20\%$. We used the MOPS backend in the mops_2208_8192_4f wide-band mode to cover a large range of molecular lines, including the 22.235120 GHz rest frequency of the $J = 6_{16} - 5_{23}$ water (H₂O) transition. The full frequency coverage is 8.8 GHz (4 sub-bands) with 8096 channels within a 2.2 GHz subband. The data were processed with the ATNF packages Livedata and Gridzilla. Livedata calibrates the spectra using ON and OFF scans and gridzilla grids all spectra into datacubes that we specified to be 0.5' per pixel, with a FWHM of 2.4' of the Mopra beam. The final channel width after regridding on a common velocity axis was 3.6 km s⁻¹. The rms noise is typically 0.01 K per channel. For Mopra, the Jy/K conversion in the K-band is 12.3 (Urquhart et al. 2010). The velocity coverage of this survey is -250 to 300 km s⁻¹.

2.3. Spitzer Data

To identify enhanced 4.5 μ m sources, we use data obtained with the *Spitzer Space Telescope* using the Infrared Array Camera (IRAC; Fazio et al. 2004). In particular, we use a combination of data from the Galactic Legacy Infrared Midplane Survey Extraordinaire (GLIMPSE; Benjamin et al. 2003) and another

IRAC survey toward the Galactic center (Stolovy et al. 2006; Arendt et al. 2008; Ramírez et al. 2008). Both data sets include data at all 4 IRAC wavelengths: 3.6, 4.5, 5.8, and 8.0 μ m. These data have an angular resolution of $\lesssim 2''$, and a pixel size of 1.2''. In total, the coverage of the survey in Galactic coordinates is $|\ell| < 65^\circ$, $|b| < 1^\circ$, with extended b coverage (up to $|b| \sim 2^\circ$) within 5° of the Galactic center.

3. Methods

3.1. Association of CH₃OH masers with Green Sources

To determine which 6.7 GHz CH₃OH masers are associated with green sources, we use an automated source detection algorithm. This algorithm uses an input list of CH₃OH maser positions to search for sources with enhanced 4.5 μ m emission ('green sources') in *Spitzer*/IRAC data. The algorithm first generates a list of candidate green sources; if the candidate green sources meet certain size and 'green' thresholds, we identify them as green sources. This new technique is based on combining two methods in which green sources are detected. One method uses ratio maps (Yusef-Zadeh et al. 2009) and the other uses an automated algorithm (Chambers et al. 2009). The details of this new algorithm are described below.

We search for green sources in a 'green ratio' image. We generate the green ratio image using: $I(4.5)/[I(3.6)^{1.2} \times I(5.8)]^{0.5}$, an empirical relation identifying sources of enhanced 4.5 μ m emission (Yusef-Zadeh et al. 2009).

To identify green sources associated with CH₃OH masers, we find contiguous pixels of enhanced 4.5 μ m emission that are above the local background and close to the maser position. 6.7 GHz CH₃OH masers are distributed in close proximity to the protostellar objects that generate them (Caswell 1997; Ellingsen 2005). As a result, we use a search radius that is comparable to the typical green source size of ~ 10 – $20''$ (e.g., Cyganowski et al. 2008; Chambers et al. 2009). Thus, for each 6.7 GHz maser, we search within a 10'' radius for a local peak in the green ratio image (R_{peak}). This same search radius of 10'' was also used by Chambers et al. (2011) to associate these two star formation indicators. An example in which a green source is detected based on this algorithm is shown in Figure 2.

To determine a local background ratio value near the position of the 6.7 GHz maser, we draw an additional aperture with a 30'' radius centered on the maser position (again, see Fig. 2). We define the local ratio background, R_{bg} , as the median value of the pixels within the annulus defined by the 10'' and 30'' apertures.

With R_{peak} and R_{bg} , we calculate the minimum ratio value, R_{cut} , required to be included as part of the candidate green source, by taking their average: $R_{cut} = [R_{peak} - R_{bg}]/2$. To find candidate green sources, we find all pixels (N_{pix}) with $R \geq R_{cut}$ that are contiguous with the peak green value (R_{peak}). In this way, we find a *candidate* green source for each 6.7 GHz maser. The contour in Figure 2 shows the pixels identified as the candidate green source.

To determine which candidate green sources are bonafide green sources, we require that they meet two more criteria: (1) a minimum number of pixels, and (2) a minimum green value threshold, calculated by taking the average green value of the background-subtracted pixels (R_{thresh}). To arrive at a value for this threshold, we use a prior known sample of green source/CH₃OH maser pairs from Chambers et al. (2011). Using green sources that were identified by eye, Chambers et al. (2011) found that 14 of the masers from C10 were associated with their visually selected sample of green sources. To opti-

¹ The Parkes and Mopra telescopes are part of the Australia Telescope, which is funded by the Commonwealth of Australia for operation as a National Facility managed by CSIRO.

² See Footnote 1.

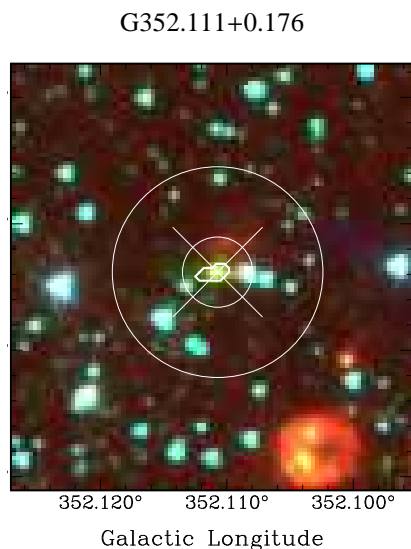


Fig. 2. *Spitzer*/IRAC 3-color image (with $8.0 \mu\text{m}$ in red, $4.5 \mu\text{m}$ in green, and $3.6 \mu\text{m}$ in blue) toward the position of a CH_3OH maser (G352.111+0.176, $v_{\text{LSR}} = -54.8 \text{ km s}^{-1}$), which is marked by the white cross sign (\times). Also shown on the image are: (1) the search radius (smaller circle) used to identify the peak ‘green’ value (R_{peak}), (2) the search radius (larger circle) used to identify find the background value (R_{bg}) (3) the contour that defines the candidate green source in the image, and (4) the position of the CH_3OH maser (\times). Note that the cross (\times) indicates only the position of the maser, and the size of the cross has no meaning.

mize our algorithm, we use a combination of number of pixels and R_{thresh} that identifies most or all of the associations found by Chambers et al. (2011), while minimizing the number of spurious associations. We find that a minimum of 9 pixels and $R_{\text{thresh}} \geq 0.2$ properly identifies 13 of the 14 (93%) green source/ CH_3OH maser pairs from Chambers et al. (2011) and finds few spurious detections. This result is shown graphically in Figure 3. Thus, we use these values to determine our final green source list from the candidate green sources.

To examine the bias in this method, we search for green sources toward random positions. These results are found in Section 4.1.1.

3.2. Identification of H_2O Masers

To identify H_2O masers in the Mopra CMZ map, we use the Clumpfind algorithm (Williams et al. 1994). Clumpfind identifies clumps by finding local peaks within a contoured data cube. Contour intervals (used to separate blended features) and lower detection limits are provided by the user, and are typically a multiple of the signal-to-noise ratio (SNR) of the data.

In order to determine an appropriate contour interval and lower limit for our Mopra data, we first analyze the SNR of the input data cube. After masking the line-free channels at each position, we calculate the noise in each spectrum, resulting in the 2-d ‘noise’ image shown in Figure 4. This 2-d image clearly shows that the noise in the Mopra H_2O data is not uniform throughout the entire cube, which is likely a result of having in different integration times in some regions, as well as varying weather during the observations. Because Clumpfind works best on data with uniform noise, we divide the original data cube by the 2-d SNR image, resulting in a data cube containing SNR values. This cube is then used as the input for Clumpfind. We find that, for the SNR data cube, a minimum threshold (i.e., detection limit) of 4 and a

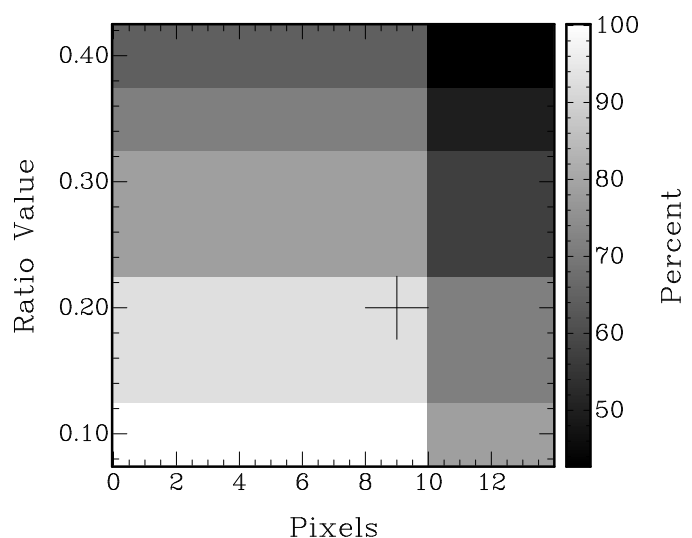


Fig. 3. Image showing the average green value vs. the number of pixels contained in candidate green sources. To determine the values used as selection criteria in our detection algorithm, we apply different combinations of these values to a known sample of green source/maser pairs to see how many the algorithm recovers. The grayscale shows the percent of known pairs recovered for each set of values. In our algorithm, we use a minimum number of 9 pixels and a mean ratio value of 0.2 as the cutoffs for green sources (marked with a black + in the image). With these values, we recover 13 of 14 (93%) green source/maser pairs.

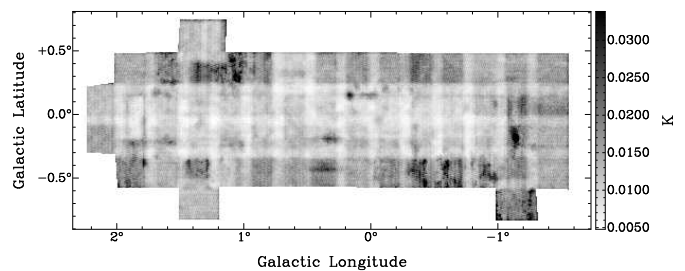


Fig. 4. Image displaying the noise in the spectrum at each position in the Mopra data cube. Because of the uneven noise throughout the data, we divide the original data cube by this 2-D image, resulting in a signal-to-noise data cube. The grayscale bar on the right shows the noise temperature in units of K (the conversion to Jy is 12.3 Jy/K).

contour interval (used to separate blended features) of 4 work best for identifying the H_2O masers in the data.

In addition to the threshold and contour levels, we also select a minimum number of volume elements (voxels) required for a source to be identified. Based on the Mopra beam size at the frequency of the H_2O maser transition (FWHM $\sim 144''$ at 22.2 GHz) and the angular size of one pixel ($30''$ by $30''$), we require a source to have at least 18 voxels to be included in our final list of masers.

4. Results

4.1. CH_3OH Masers and Green Sources

C10 detect 183 CH_3OH masers in their survey region ($6^\circ < \ell < 345^\circ$, $|b| < 2^\circ$), with a 1σ detection limit of 0.07 Jy . Histograms of the maser distribution as a function of ℓ and b can be seen in Figure 5. The distribution in Galactic latitude shows that the masers have a roughly Gaussian distribution,

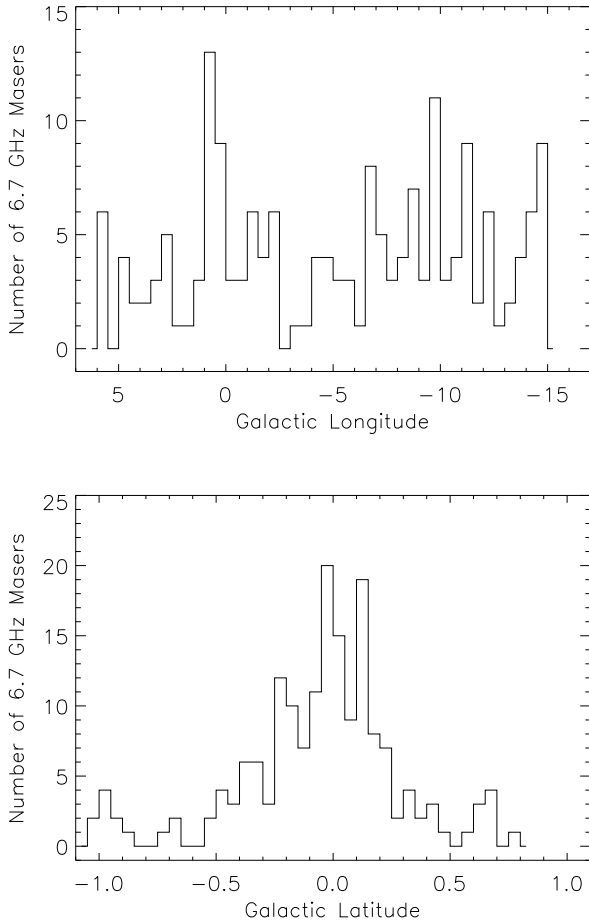


Fig. 5. *Top:* Histogram of the distribution of 6.7 GHz masers in Galactic longitude (integrated over all Galactic latitudes). The bin size is 1.5° . The peak of the distribution is largely due to the cluster of 11 masers in Sgr B2. *Bottom:* Histogram of the distribution of 6.7 GHz masers in Galactic latitude (integrated over all Galactic longitudes). The bin size is 0.15° . The masers are distributed around the Galactic equator.

centered on the Galactic plane. The Galactic longitude distribution displays a peak toward the Galactic center, mostly due to a large number of masers in the Sgr B star forming region. Figure 6 contains a 2-D image of the maser distribution, and clearly shows the peak of the maser distribution in Sgr B.

We run the green source detection algorithm (described above) on 175 of the 183 masers in the C10 catalog (8 were excluded because we do not have corresponding IRAC data). We find that $86/175$ ($49.1 \pm 5.3\%$) of the 6.7 GHz masers are associated with a green source. These green sources range in size (in the $1.2''$ by $1.2''$ IRAC pixels) from 9 (the minimum based on our detection method) to 517, with a median of 17 IRAC pixels (see Fig. 7).

A summary of these results can be found in Table 1, which lists, for each CH_3OH maser, the maser name (Column 1; from C10), the velocity of peak maser emission (Column 2; from C10), the Galactic longitude, latitude and value for the peak green pixel in each green source candidate, R_{peak} (Columns 3, 4, and 5), the background green value near each green source candidate, R_{bg} (Column 6), the green value used to define the boundary of the green source candidate, R_{cut} (Column 7), the average green value for the pixels within the green source can-

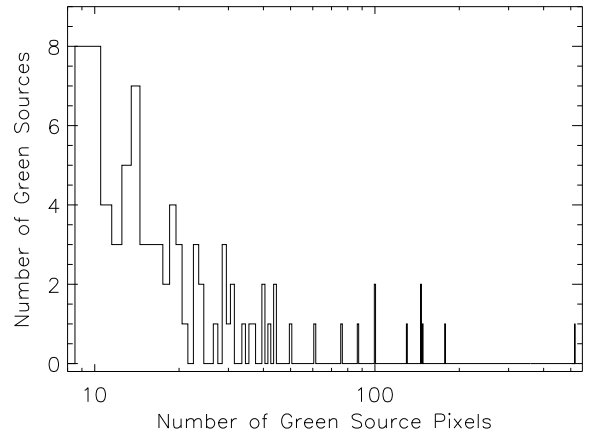


Fig. 7. Histogram of the number of pixels in the green sources associated with 6.7 GHz CH_3OH masers. The sizes (in IRAC pixels) range from 9 (the minimum based on our detection method) to 517, with a median of 17.

didate, R_{thresh} (Column 8), and the number of pixels, N_{pix} , in the green source candidate (Column 9). The final column in Table 1 contains a flag ('Y' or 'N'; Column 10) to indicate if a green source is associated with a CH_3OH maser based on the values in Columns 3 through 9.

Using these detected sources, we calculate the detection rates for green sources toward 6.7 GHz masers as a function of Galactic longitude and latitude. In Figure 8, we show that the longitude distribution of detection rates varies between 20% and 86%, with typical errors of $\sim 20\%$. The distribution shows possible enhancements at $\ell \sim -2^\circ$ and $\ell \sim -8^\circ$, and a depressed rate at $\ell \sim -5^\circ$. The distribution of green source detection rates as a function of Galactic latitude, shown in Figure 8, shows a clear deficit of green sources detected near the midplane ($b \sim 0^\circ$) of the Galaxy. The central 0.3° has a detection rate of $\sim 35 \pm 10\%$, while the regions with $|b| > 0.5^\circ$ have detection rates of $> 50\%$, with some bins at 100%.

Because we want to compare Galactic center candidate sources to Galactic disk sources, we need a method (or methods) to estimate the distances to the sources. To determine if the green sources are foreground or Galactic center sources, we use their Galactic coordinates with respect to the Galactic plane and their corresponding maser velocities. First, we use the Galactic coordinates of the sources to separate our sources into GC sources and non-GC sources. To cover the CMZ, and to match the scale height of young stellar objects in the Galactic center region (Yusef-Zadeh et al. 2009), we define the GC region to be $|\ell| < 1.3^\circ$, $|b| < 10'$. Using these criteria for distance, we find that $8/23$ GC CH_3OH masers ($34.8 \pm 12.3\%$) are associated with green sources, and $78/152$ ($51.3 \pm 5.8\%$) non-GC CH_3OH masers are associated with green sources. These association rates are listed in Table 2, which lists the method of distance estimation in Column 1, the location of the masers in Column 2, the number of CH_3OH masers at that distance in Column 3, the number of those masers that are associated with green sources in Column 4, and the association rate calculated on those numbers in Column 5. Figure 9 shows the positions of the CH_3OH masers, their assigned locations (based on their Galactic coordinates), and the velocities of the peak maser emission.

Next, we use the distance estimates made by C10, who based their estimates on the velocities of the CH_3OH masers and a

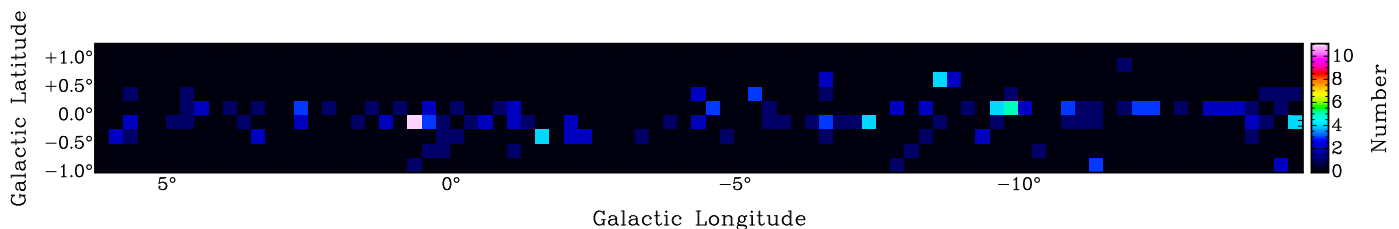


Fig. 6. Distribution of the 6.7 GHz masers from C10. The pixel size is 0.25° . The bright peak at $(\ell, b) = (0.66, -0.04)$ is from a cluster of masers in Sgr B2.

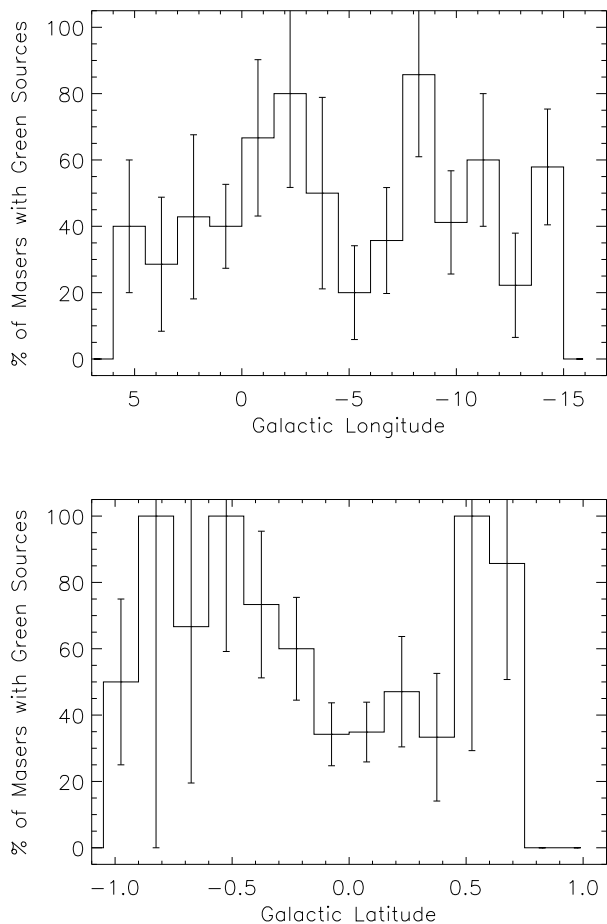


Fig. 8. *Top:* Histogram of the percentage of 6.7 GHz masers associated with green sources as a function of Galactic longitude. *Bottom:* Histogram of the percentage of 6.7 GHz masers associated with green sources as a function of Galactic latitude. The bin size is 0.15° . Errors for the detection rates in both histograms are calculated using \sqrt{N} counting statistics.

model of circular Galactic rotation (and allowing for small deviations; see C10 for more details). In short, some maser velocities are consistent with Galactic rotation models, and are placed outside the GC region. Other masers have velocities consistent with a location within the 3 kpc arms, and are assigned that location. Those masers that fit neither of these categories, and have $|\ell| < 1.3^\circ$ (with no restriction in Galactic latitude) are placed at the distance of the GC. Using these criteria for distance, we find that 13/27 GC CH_3OH masers ($48.1 \pm 13.3\%$) are associated

Table 2. Association Rates of CH_3OH Masers with Green Sources

Distance Method	Galactic Location	CH_3OH Masers	Green Source Associations	Association Rate
Position ^a	GC	23	8	$34.8 \pm 12.3\%$
	Disk	152	78	$51.3 \pm 5.8\%$
Velocity ^b	GC	27	13	$48.1 \pm 13.3\%$
	Disk	148	73	$49.3 \pm 5.8\%$
Both	GC	17	4	$23.5 \pm 11.8\%$
	Disk	158	82	$51.9 \pm 5.7\%$
Total		175	86	$49.1 \pm 5.3\%$

Notes. ^(a) Based on Galactic coordinates, with $|\ell| < 1.3^\circ$ and $|b| < 10'$ defining the GC region (see Section 4.1). ^(b) Based on the velocities of the masers and a model of circular Galactic rotation (see Section 4.1).

with green sources, and 73/148 ($49.3 \pm 5.8\%$) non-GC CH_3OH masers are associated with green sources.

Finally, we also look at the subset of sources that meet the position (by Galactic coordinates) *and* velocity criteria described above. These masers all have positions with $|\ell| < 1.3^\circ$, $|b| < 10'$, and velocities that are inconsistent with both standard Galactic rotation and placement in the 3 kpc arms. Using these criteria for distance, we find that 4/17 GC CH_3OH masers ($23.5 \pm 11.8\%$) are associated with green sources, and 82/158 ($51.9 \pm 5.7\%$) non-GC CH_3OH masers are associated with green sources.

4.1.1. Random Test

To determine if the association rates are true associations of green sources with 6.7 GHz masers or simply chance alignments of the two star formation indicators, we placed test masers in the survey longitude and latitude ranges and searched for green sources using the same method described above. Because the C10 CH_3OH masers are roughly evenly distributed in longitude, our test masers have a uniform distribution in longitude. To match the latitude distribution of masers seen in Figure 5, we fit a Gaussian to the distribution and used its parameters to generate the Galactic latitude distribution of test masers. We placed 175 test masers in the survey region, to match the number of masers in the C10 catalog. To increase the statistics, we ran the test a total of ten times. We find a test maser-green source association rate of $1.3 \pm 0.3\%$ for our total sample of 1,750 test masers. Thus, we consider the chances of our detection rates being contaminated by random chance associations to be small.

4.2. H_2O Masers

Using the Clumpfind detection algorithm as described in Section 3.2, we find a total of 37 H_2O masers. These masers are listed in Table 3, which contains the identification numbers (Col-

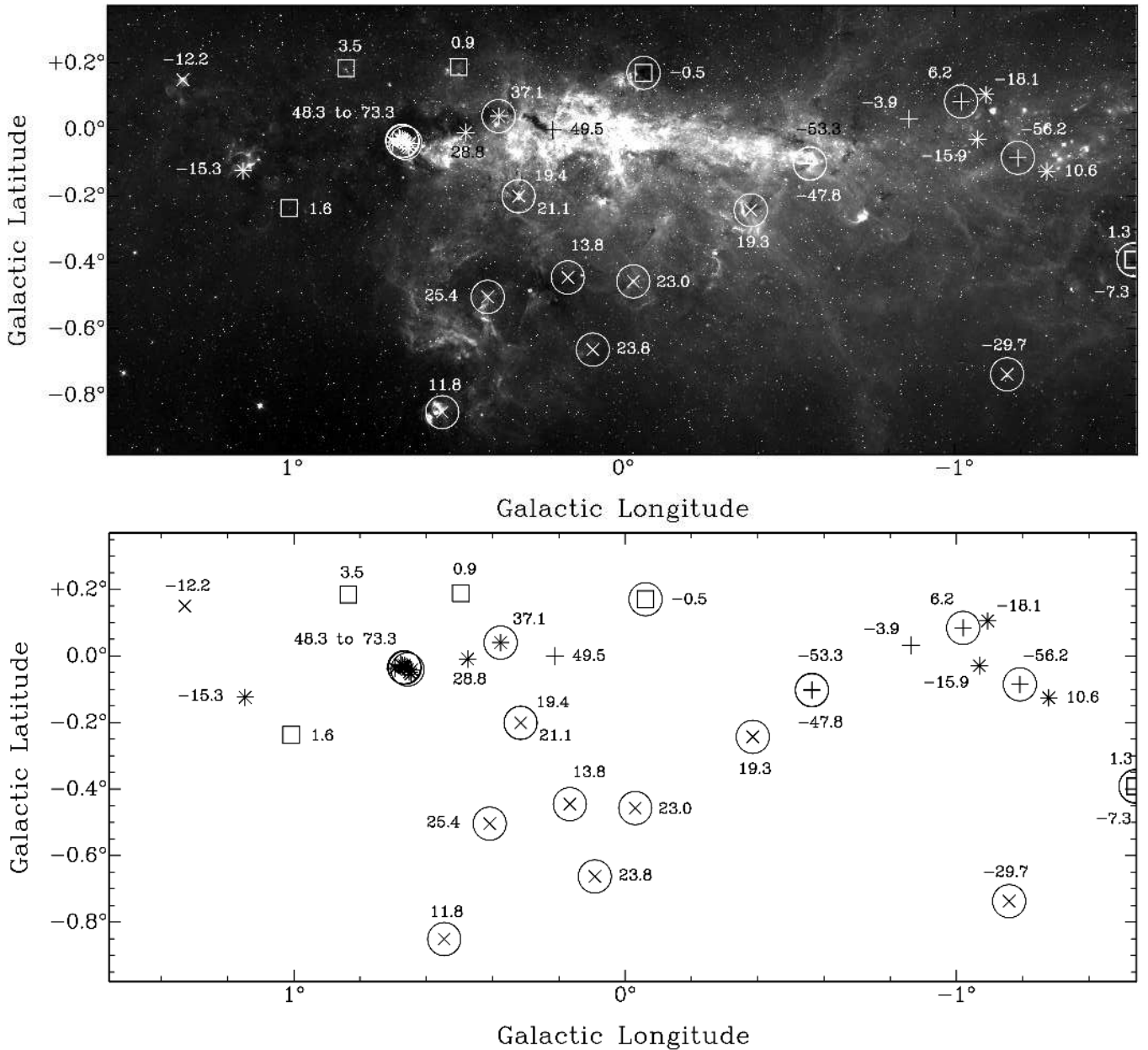


Fig. 9. *Top:* *Spitzer*/IRAC 8 μm image of the Galactic center region showing 6.7 GHz CH₃OH masers. Crosses (+) indicate the positions of 6.7 GHz CH₃OH masers placed in the Galactic center region based on position. The \times symbols indicate the positions of 6.7 GHz CH₃OH masers placed in the Galactic center region based on velocity. The asterisks (*) indicate the positions of 6.7 GHz CH₃OH masers placed in the Galactic center region based on both distance criteria. The squares show the locations of the masers thought to reside in the disk. Sources that are circled are associated with an enhanced 4.5 μm emission source. Each maser is labelled with the velocity (in km s⁻¹) of the peak maser emission. *Bottom:* Same as the *top* figure, but with a blank background instead of the 8 μm image.

umn 1), the Galactic coordinates of the masers (Columns 2 and 3), the velocity of peak emission for each maser (Column 4), the peak intensities of the masers (Column 5), and the number of voxels in the source (Column 6). The peaks range from 52 mK to 9.54 K, with an average of 1.02 K and a median of 160 mK, and the velocities range from -208.5 to 129.4 km s⁻¹. Spectra of all 37 detections can be seen in Figure 10. The distribution of the water masers as a function of Galactic longitude and latitude can be seen in Figure 11. In Figure 12, the positions of the water masers are overplotted on an image of the Galactic center region, along with the velocities of the peak maser emission. Some masers share the same positions but have different velocities. These likely comprise a cluster of masers, but higher

angular resolution observations are needed to determine their positions more precisely.

The most notable feature in these distributions is the peak of H₂O masers at $\ell \sim 0.6^\circ$, which can be attributed to the H₂O maser emission from Sgr B2. We detect a total of 9 H₂O masers toward Sgr B, including the three strongest emission features in the survey. Figure 13 shows a spectrum toward Sgr B that indicates the velocities of these 9 masers, which are spread from ~ 0 to ~ 140 km s⁻¹.

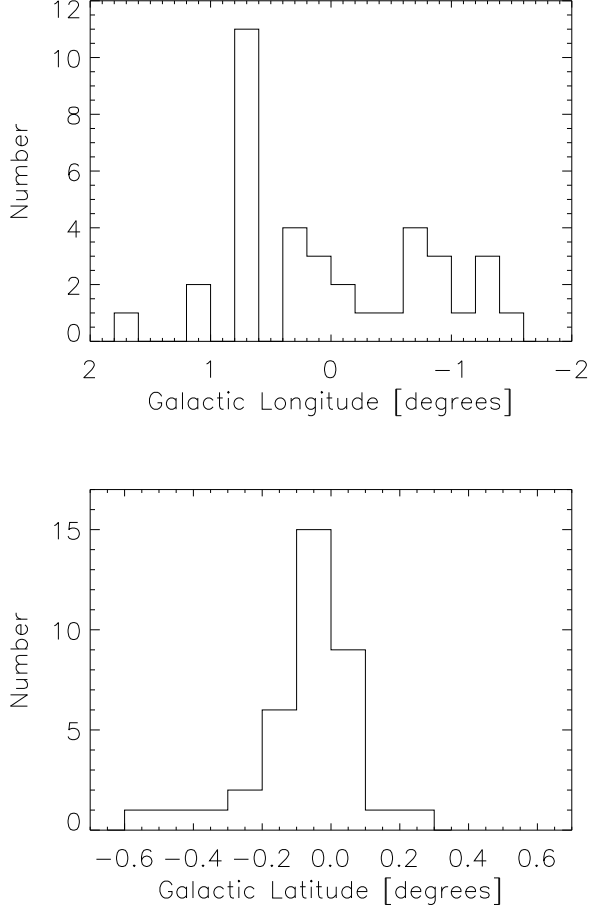


Fig. 11. Distribution of the Mopra H₂O masers as a function of Galactic longitude (*top*) and latitude (*bottom*). The peak of the longitude distribution is due to the 9 masers associated with Sgr B.

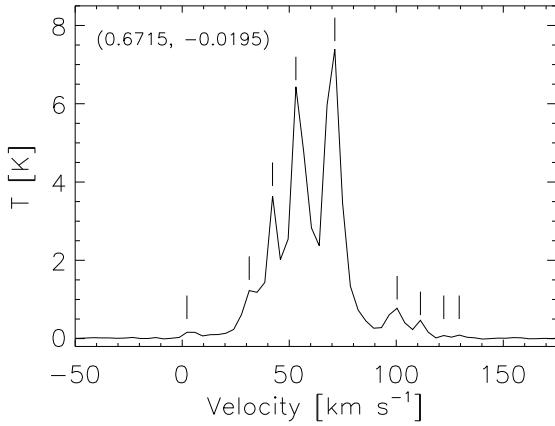


Fig. 13. Mopra H₂O maser spectrum toward Sgr B. The position of the spectrum (in ℓ, b) is printed at the top of the plot. The vertical lines indicate the velocities of masers identified by the Clumpfind routine. The velocities of the masers identified are 2.2, 31.3, 42.2, 53.1, 71.3, 100.4, 111.3, 122.2, and 129.4 km s⁻¹. The conversion to Jy is 12.3 Jy/K.

Table 3. H₂O Masers in the Survey Region

Number	ℓ^a ($^\circ$)	b^a ($^\circ$)	v^a (km s ⁻¹)	T_{peak} (K)	Number of Voxels
1	0.663	-0.036	71.3	9.54	1703
2	0.663	-0.019	53.1	6.48	1766
3	0.671	-0.019	42.2	3.64	893
4	-0.854	0.031	-1.4	5.08	372
5	-0.862	0.031	-1.4	5.01	446
6	0.671	-0.019	31.3	1.23	645
7	0.671	-0.019	100.4	0.77	673
8	0.380	0.047	38.6	0.78	218
9	-1.337	-0.053	-8.7	0.74	174
10	0.671	-0.019	111.3	0.47	243
11	1.138	-0.128	-19.6	0.46	158
12	-1.337	-0.053	-15.9	0.44	280
13	0.055	-0.219	13.2	0.54	93
14	-0.570	-0.103	-59.5	0.21	117
15	-0.679	-0.036	-110.4	0.16	79
16	0.671	-0.019	2.2	0.16	200
17	0.613	0.006	9.5	0.16	104
18	-0.704	0.031	-1.4	0.11	161
19	-1.337	-0.036	2.2	0.16	67
20	0.155	-0.561	-70.4	0.20	76
21	-0.862	0.031	-12.3	0.16	81
22	0.205	-0.011	-15.9	0.09	69
23	1.163	-0.019	-19.6	0.08	35
24	0.763	-0.253	-48.6	0.09	45
25	-0.662	0.281	-1.4	0.16	43
26	0.371	0.031	16.8	0.08	59
27	0.196	-0.153	45.9	0.06	34
28	-1.104	0.022	-15.9	0.13	26
29	-0.720	0.164	53.1	0.06	26
30	0.671	-0.019	129.4	0.09	36
31	-0.070	-0.153	-8.7	0.07	57
32	-0.070	-0.144	-19.6	0.07	21
33	-0.245	-0.378	-59.5	0.10	23
34	0.671	-0.019	122.2	0.08	22
35	-1.462	-0.194	-208.5	0.07	19
36	0.205	0.006	42.2	0.05	24
37	1.705	-0.486	-37.7	0.06	19

Notes. (^a) Values of ℓ, b , and v are extracted from the Mopra data cube, which has a pixel size of 0.5' and a channel width of ~ 3.6 km s⁻¹.

4.2.1. Association of H₂O and CH₃OH Masers

To associate H₂O and CH₃OH masers, we search for H₂O masers that are within one Mopra beam ($\sim 144''$) of CH₃OH masers. Figure 14 shows the positions of H₂O and CH₃OH masers overlaid on an image of the GC region. The positions of the H₂O masers are marked by circles that match the Mopra beam size. Crosses mark the positions of CH₃OH masers (the size of the crosses has no physical meaning). We consider a H₂O and CH₃OH maser to be associated when the center of the cross falls within the circle marking the Mopra beam at the H₂O maser frequency.

These results, including the velocity information of the masers, are also shown in Table 4. Columns 1-3 of the table list the CH₃OH maser name (from C10), and the lower and upper velocity limits of the CH₃OH maser emission (from C10). In Columns 4-7, we list the properties of the H₂O masers that are associated with the CH₃OH masers—the H₂O maser numbers, their Galactic coordinates, and the velocity of their peak

emission. Column 8 lists the angular separation between the associated CH₃OH and H₂O masers. Column 9 indicates if the CH₃OH maser is associated with a green source. If a CH₃OH maser is associated with multiple H₂O masers, then the CH₃OH maser information is printed only once, and a line for each of the H₂O masers is printed.

Because 22 GHz H₂O masers are found in shocks and outflows, their velocities may not match the velocities of the radiatively excited 6.7 GHz CH₃OH masers. Therefore, we do not use the velocities of the masers as association criteria. The velocities of both types of masers are listed in Table 4.

Some of the H₂O masers are associated with more than one CH₃OH maser. Without higher angular resolution, we are unable to tell if the masers are exactly coincident or are just nearby to one another. Nevertheless, we include these associations, along with whether or not the CH₃OH maser is coincident with a green source, to examine the star formation in the CMZ, as well as to determine candidates for potential follow-up observations at higher angular resolution.

Of the 175 CH₃OH masers in the C10 catalog, 39 fall within the Mopra H₂O maser survey region. Of these 39, 15 are associated with H₂O masers, while 24 are not. The list of these 15 CH₃OH masers can be found in the first column of Table 4.

There are a total of 37 H₂O masers in the Mopra survey region, 18 of which are associated with CH₃OH masers. These H₂O masers, along with their identification number, can be found in Table 4. Because H₂O masers can be associated with more than one CH₃OH masers, some of the H₂O masers are listed more than once in this table. For completeness, we also include Table 5, which lists CH₃OH masers that are not associated with H₂O masers. The first three columns of Table 5 contain the name and Galactic coordinates of the CH₃OH masers (from C10), Columns 4 and 5 contain the minimum and maximum velocities of the maser features (from C10), the peak intensity of the maser emission is in Column 6, and the last column contains a flag indicating if the CH₃OH maser is associated with a green source. Many of the CH₃OH masers in this list are outside of the Mopra H₂O maser survey region. In addition, we list H₂O masers that are not associated with CH₃OH masers in Table 6. The columns in this table are: (1) the number of the identified H₂O maser, (2) the Galactic longitude of the maser, (3) the Galactic latitude of the maser, (4) the velocity of the peak emission from the maser, and (5) the peak emission of the maser. It is interesting to note that each of the 8 strongest H₂O masers (numbers 1 through 8 in Table 3) are associated with CH₃OH masers, and are thus not included in Table 6.

5. Discussion

5.1. Association Rate as a Function of Galactic Longitude

To search for trends in the association rate of 6.7 GHz masers and 4.5 μ m emission, we binned the sources (and association rates) by Galactic Longitude. The results are shown in Figure 8. The association rate varies from bin to bin (from $20 \pm 14\%$ to $85 \pm 25\%$), but we find no strong trend with Galactic longitude. There appears to a decrement of associations at $\ell \sim -5^\circ$, and enhancements of associations at $\ell \sim -2^\circ$ and -8° . Because of the large error bars and the large bin-to-bin variations, we consider the likely cause of these to be the results of small number statistics and binning.

Table 6. H₂O Masers not Associated with CH₃OH Masers

Number	ℓ^a ($^\circ$)	b^a ($^\circ$)	v^a (km s ⁻¹)	T_{peak} (K)
9	-1.337	-0.053	-8.7	0.74
12	-1.337	-0.053	-15.9	0.45
13	0.055	-0.220	13.2	0.54
15	-0.678	-0.036	-110.4	0.16
17	0.613	0.005	9.5	0.16
18	-0.704	0.030	-1.4	0.11
19	-1.337	-0.036	2.2	0.16
20	0.155	-0.561	-70.4	0.20
23	1.163	-0.019	-19.6	0.08
24	0.763	-0.253	-48.6	0.09
25	-0.662	0.281	-1.4	0.16
27	0.197	-0.153	45.9	0.06
28	-1.103	0.022	-15.9	0.13
29	-0.720	0.164	53.1	0.06
31	-0.070	-0.153	-8.7	0.07
32	-0.070	-0.144	-19.6	0.07
33	-0.245	-0.378	-59.5	0.10
35	-1.462	-0.195	-208.5	0.07
37	1.705	-0.486	-37.7	0.07

Notes. ^(a) Values of ℓ , b , and v are extracted from the Mopra data cube, which has a pixel size of 0.5' and a channel width of ~ 3.6 km s⁻¹.

5.2. Association Rate as a Function of Galactic Latitude

We find that CH₃OH masers near the Galactic midplane ($|b| < 10'$) are less likely ($34.8 \pm 6.4\%$) to be associated with green sources than those above or below it ($62.9 \pm 8.4\%$). While this could be a real effect, and masers outside the midplane could simply have higher association rates with 4.5 μ m sources than those in the midplane, we find it much more likely to be an optical depth effect of having two star formation tracers at very different wavelengths/frequencies.

The Galactic plane is optically thin at 6.7 GHz, making it possible to detect 6.7 GHz CH₃OH masers throughout the Galaxy, including the far side of the Galactic plane. This is not the case, however, for 4.5 μ m emission. At this much shorter wavelength, extinction plays a much larger role (see, e.g., Pandey & Mahra 1987), preventing the detection of green sources on the far side of the Galaxy (behind, e.g., the molecular clouds on the near side of the Galaxy). Because the extinction is higher in the Galactic plane, we are likely to have a cleaner line of sight to 6.7 GHz masers that reside above or below the Galactic plane. Thus, we find a lower association rate of 4.5 μ m emission with 6.7 GHz CH₃OH masers for sources that are in the midplane of the Galaxy ($l < 10'$) than those above or below it.

5.3. Comparing the Galactic Center with the Galactic Disk

To see how star formation in the Galactic center region may differ from that of the disk, we compare the 6.7 GHz CH₃OH association rate with enhanced 4.5 μ m emission. As described in Section 4.1, we make three different distance estimates based on the positions of the masers, the velocities of the masers, and the combination of these two criteria.

Using Galactic coordinates alone ($|\ell| < 1.3^\circ$, $|b| < 10'$) to estimate the distances to the CH₃OH masers, and assuming that all masers that fit the distance criteria are indeed in the GC (and not the foreground), we find that $34.8 \pm 12.3\%$ are associ-

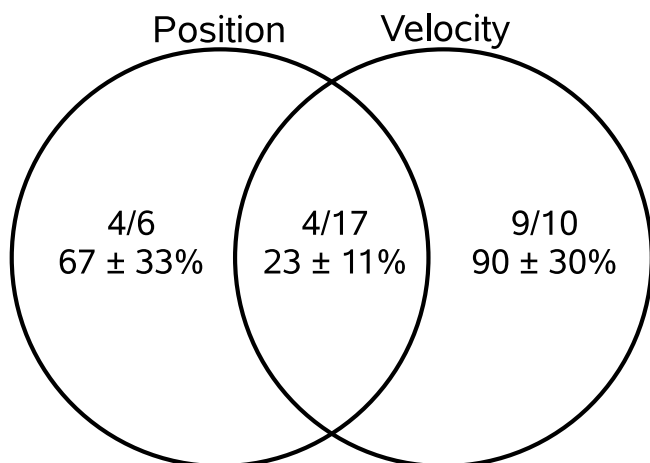


Fig. 15. Diagram showing green source detection rates based on two different distance estimates. Sources placed in the Galactic center based on position all have $|\ell| < 1.3^\circ$ and $|b| < 10'$. Distance estimates based on velocity are taken from C10. For comparison, the green source detection rates for masers that are not at the distance of the Galactic center (based on position or velocity) is $48.6 \pm 5.9\%$ (69/142).

ated with green sources in the GC, and that $51.3 \pm 5.8\%$ of disk sources are associated with green sources. The association rate for the disk includes all Galactic latitudes. Because the GC is in the Galactic midplane, however, we should compare the GC association rate to the association rate in the rest of the midplane ($6^\circ < \ell < 345^\circ$), excluding the GC longitudes ($|\ell| < 1.3^\circ$). When we do this, we find that the disk midplane association rate is $34.9 \pm 7.4\%$, very close to the association rate for the GC. Thus, we find no differences between the two regions using position alone as a distance indicator.

When we use only the source velocity to estimate the locations of the masers, we find nearly identical association rates between the CH_3OH masers and the enhanced $4.5 \mu\text{m}$ emission sources in the GC ($48.1 \pm 13.3\%$) and the disk ($49.3 \pm 5.8\%$). Because the positions of the masers are not considered in this distance estimate, no adjustment for the midplane is necessary. The similar association rates again point to no significant difference between the GC and disk regions.

Using both positional and velocity criteria to place sources at the distance of the Galactic center, we find a detection rate ($23.5 \pm 11.8\%$) that is lower than that of all other midplane sources ($34.9 \pm 7.4\%$). While the association rate in the GC is lower using both distance criteria, the large error bars keep this from being a significant result. When we look at the sources placed in the GC region by only *one* of the two indicators (position *or* velocity), we find that they have high association rates, $66.7 \pm 33.3\%$ for those sources whose positions match the GC, and $90.0 \pm 30.0\%$ for those whose velocities match the GC. Figure 15 shows a diagram with these association rates. These elevated rates could simply be a result of small number statistics, since when taking into account their error bars, they are consistent with the disk association rate, especially at larger Galactic latitudes. Nevertheless, this difference remains intriguing.

As described in Section 2.2, the Mopra H_2O survey covered the region $-1.5^\circ < \ell < 2^\circ$, $-0.6^\circ < b < 0.5^\circ$ with a velocity coverage of -250 to 300 km s^{-1} . This covers the entire CMZ, with only limited coverage outside of the CMZ. Nevertheless, we can compare the H_2O masers in the CMZ to those outside

the CMZ, as determined by their positions. We find that of the 27 H_2O masers in the CMZ, 18 are associated with CH_3OH masers ($67 \pm 16\%$). Outside of the CMZ, we find that none of the 10 H_2O masers are associated with CH_3OH masers. Thus, there appears to be a significant difference between the H_2O masers in these regions. As discussed above, the H_2O maser emission from Sgr B2 is the dominant feature of the survey. Even if we remove the 9 Sgr B2 H_2O masers (all of which are associated with CH_3OH masers), the difference persists ($50 \pm 17\%$).

It is important to note that H_2O masers are also found toward AGB stars. These H_2O masers tend to be less luminous than those found toward high-mass star forming regions (Palagi et al. 1993; Caswell et al. 2011). Indeed, in a 0.5 deg^2 H_2O maser survey of the Galactic center, Caswell et al. (2011) found that only 3 of their 27 detected masers could be definitely attributed to AGB stars. Using this detection rate, of the 37 H_2O masers detected in our Mopra survey, ~ 4 may be associated with evolved AGB stars rather than sites of star formation. The H_2O masers associated with CH_3OH masers or green sources are very unlikely to also be associated with AGB stars. Thus, the effect of the small number of AGB H_2O masers in our sample is negligible.

The fact that we do not find any CH_3OH masers toward the H_2O masers outside the CMZ is intriguing, and may be related to a different timescale of star formation inside the CMZ when compared to the Galactic disk. While still somewhat speculative, some recent work (Ellingsen et al. 2007; Breen et al. 2010) has proposed an evolutionary sequence of CH_3OH masers in which Class I CH_3OH masers, generated by protostellar outflows, are formed before radiatively excited Class II CH_3OH masers (e.g., the 6.7 GHz CH_3OH maser). In addition, some observations have suggested that the 22 GHz H_2O maser also arises in an early phase of star formation and overlaps with the Class I CH_3OH masers, in particular toward green sources (e.g., Chambers et al. 2009). Thus, if we assume that the 22 GHz H_2O masers arise at an earlier evolutionary state than the 6.7 GHz CH_3OH masers, then perhaps the much higher correlation rate of the two masers in the GC (67% vs 0%) corresponds to a longer overlap period of the two stages, and possibly a compressed timescale of star formation in the GC relative to that of the disk. This speculative result can be tested using higher-resolution H_2O maser data to verify the GC correlations, a larger number of H_2O and CH_3OH masers in the GC (from more sensitive surveys), as well as large co-spatial surveys of H_2O and CH_3OH masers in the Galactic plane to better establish the correlation rate in the disk.

5.4. Asymmetry in the H_2O Maser Distribution around the Galactic Center

Yusef-Zadeh et al. (2009) found an asymmetry in the distribution of young stellar object (YSO) candidates as probed by $24 \mu\text{m}$ sources, with a larger number of YSO candidates with $\ell < 0$ relative to $\ell > 0$. The distribution of H_2O masers as a function of Galactic longitude seen in Figure 11 shows no obvious asymmetry with respect to $\ell = 0$, with 19 masers having $\ell > 0$ and 18 masers having $\ell < 0$. The most striking feature in this distribution of H_2O masers is the peak at $\sim \ell = 0.7$, which is almost entirely due to masers in Sgr B2 (10 of the 11 masers in the bin have coordinates that place them within Sgr B2). If we remove these 10 masers from the distribution, we find that there are 11 H_2O masers with $\ell > 0$, and 16 with $\ell < 0$, consistent with the asymmetry found by Yusef-Zadeh et al. (2009). One explanation for the asymmetry offered by Yusef-Zadeh et al. (2009)

was that higher extinction due to dense clouds may be responsible for the asymmetry in the distribution of 24 μm sources. Extinction is not a problem at the frequency of the H_2O masers, suggesting that the asymmetry may be a real feature. The larger numbers of both 24 μm sources and H_2O masers at $\ell < 0$ indicate an enhancement of on-going star formation in this region.

6. Conclusions

We present the results of our study of star formation in the CMZ and how it compares to the Galactic disk. We make our comparison through the correlation of 6.7 GHz CH_3OH masers, 22 GHz H_2O masers, and green sources. As part of this study, we developed an automated algorithm to identify regions of extended, enhanced 4.5 μm emission toward 6.7 GHz CH_3OH masers. This new technique can be a powerful tool to trace regions of star formation provided the column density along the line of sight is not too high. Moreover, we used the Mopra telescope to survey the 22 GHz H_2O maser emission in the CMZ, resulting in the detection of 37 individual water masers.

We find that the association rate of CH_3OH masers with green sources as a function of Galactic longitude is relatively flat. In Galactic latitude, on the other hand, we find that there is a significant decrease in the association rate along the Galactic midplane, which is likely an infrared extinction effect. Using two different distance estimates, we do not detect any significant difference in the association rates of green sources with CH_3OH masers between the Galactic center and the disk. This suggests that once the star formation process has begun, its observational signatures are similar in the GC and the Galactic disk, despite the different physical conditions of the gas in the two regions.

We find that the H_2O masers in our survey are much more likely to be associated with a CH_3OH maser if they are located in the Galactic center rather than the Galactic disk. Indeed, we find zero H_2O masers (out of 10) associated with CH_3OH masers outside the Galactic center region. This may indicate a different timescale of star formation in the GC when compared to the Galactic disk. Future high angular resolution observations of the newly detected H_2O masers are needed to better establish the positions of the H_2O masers and test this result.

Acknowledgements. Acknowledgements to be included.

References

Ao, Y., Henkel, C., Menten, K. M., et al. 2013, *A&A*, 550, A135
 Arendt, R. G., et al. 2008, *ApJ*, 682, 384
 Benjamin, R. A., et al. 2003, *PASP*, 115, 953
 Breen, S. L., Ellingsen, S. P., Caswell, J. L., & Lewis, B. E. 2010, *MNRAS*, 401, 2219
 Caswell, J. L. 1997, *MNRAS*, 289, 203
 Caswell, J. L., et al. 2010, *MNRAS*, 404, 1029
 Caswell, J. L., Breen, S. L., & Ellingsen, S. P. 2011, *MNRAS*, 410, 1283
 Chambers, E. T., Jackson, J. M., Rathborne, J. M., & Simon, R. 2009, *ApJS*, 181, 360
 Chambers, E. T., Yusef-Zadeh, F., & Roberts, D. 2011, *ApJ*, 733, 42
 Chen, X., Ellingsen, S. P., & Shen, Z.-Q. 2009, *MNRAS*, 396, 1603
 Claussen, M. J., Marvel, K. B., Wootten, A., & Wilking, B. A. 1998, *ApJ*, 507, L79
 Cox, P., & Launeis, R. 1989, *The Center of the Galaxy*, 136, 121
 Cragg, D. M., Johns, K. P., Godfrey, P. D., & Brown, R. D. 1992, *MNRAS*, 259, 203
 Cyganowski, C. J., et al. 2008, *AJ*, 136, 2391
 Cyganowski, C. J., Brogan, C. L., Hunter, T. R., & Churchwell, E. 2009, *ApJ*, 702, 1615
 De Buizer, J. M., & Vacca, W. D. 2010, *AJ*, 140, 196
 Elitzur, M., Hollenbach, D. J., & McKee, C. F. 1989, *ApJ*, 346, 983
 Ellingsen, S. P. 2005, *MNRAS*, 359, 1498

Ellingsen, S. P., Voronkov, M. A., Cragg, D. M., Sobolev, A. M., Breen, S. L., & Godfrey, P. D. 2007, *IAU Symposium*, 242, 213
 Fazio, G. G., Hora, J. L., Allen, L. E., et al. 2004, *ApJS*, 154, 10
 Fazio, G. G., Hora, J. L., Allen, L. E., et al. 2004, *ApJS*, 154, 10
 Ferrière, K., Gillard, W., & Jean, P. 2007, *A&A*, 467, 611
 Foster, J. B., Jackson, J. M., Chambers, E. T., & Stojimirovic, I. 2010, *ApJ*, submitted.
 Furuya, R. S., Kitamura, Y., Wootten, H. A., Claussen, M. J., & Kawabe, R. 2001, *ApJ*, 559, L143
 Genzel, R., Downes, D., Moran, J. M., et al. 1978, *A&A*, 66, 13
 Jwinn, C. R. 1994, *ApJ*, 429, 241
 Hollenbach, D., Elitzur, M., & McKee, C. F. 2013, *ApJ*, 773, 70
 Houghton, S., & Whiteoak, J. B. 1995, *MNRAS*, 273, 1033
 Huettemeister, S., Dahmen, G., Mauersberger, R., et al. 1998, *A&A*, 334, 646
 Immer, K., Menten, K. M., Schuller, F., & Lis, D. C. 2012, *A&A*, 548, A120
 Jones, P. A., Burton, M. G., Tohill, N. F. H., & Cunningham, M. R. 2011, *MNRAS*, 411, 2293
 Jones, P. A., Burton, M. G., Cunningham, M. R., et al. 2012, *MNRAS*, 419, 2961
 Jones, P. A., Burton, M. G., Cunningham, M. R., Tohill, N. F. H., & Walsh, A. J. 2013, *MNRAS*, 433, 221
 Kennicutt, R. C., Jr. 1998, *ARA&A*, 36, 189
 Longmore, S. N., Rathborne, J., Bastian, N., et al. 2012, *ApJ*, 746, 117
 Marston, A. P., Reach, W. T., Noriega-Crespo, A., et al. 2004, *ApJS*, 154, 333
 Martín-Pintado, J., de Vicente, P., Rodríguez-Fernández, N. J., Fuente, A., & Planesas, P. 2000, *A&A*, 356, L5
 Menten, K. M. 1991, *ApJ*, 380, L75
 Mills, E. A. C., & Morris, M. R. 2013, *ApJ*, 772, 105
 Pandey, A. K., & Mahra, H. S. 1987, *MNRAS*, 226, 635
 Minier, V., Ellingsen, S. P., Norris, R. P., & Booth, R. S. 2003, *A&A*, 403, 1095
 Molinari, S., Bally, J., Noriega-Crespo, A., et al. 2011, *ApJ*, 735, L33
 Morris, M., & Serabyn, E. 1996, *ARA&A*, 34, 645
 Noriega-Crespo, A., Morris, P., Marleau, F. R., et al. 2004, *ApJS*, 154, 352
 Norman, C., & Silk, J. 1979, *ApJ*, 228, 197
 Odenwald, S. F., & Fazio, G. G. 1984, *ApJ*, 283, 601
 Oka, T., Geballe, T. R., Goto, M., Usuda, T., & McCall, B. J. 2005, *ApJ*, 632, 882
 Palagi, F., Cesaroni, R., Comoretto, G., Felli, M., & Natale, V. 1993, *A&AS*, 101, 153
 Pierce-Price, D., et al. 2000, *ApJ*, 545, L121
 Ramírez, S. V., Arendt, R. G., Sellgren, K., Stolovy, S. R., Cotera, A., Smith, H. A., & Yusef-Zadeh, F. 2008, *ApJS*, 175, 147
 Rathborne, J. M., Jackson, J. M., Chambers, E. T., Simon, R., Shipman, R., & Frieswijk, W. 2005, *ApJ*, 630, L181
 Rathborne, J. M., Jackson, J. M., & Simon, R. 2006, *ApJ*, 641, 389
 Riquelme, D., Bronfman, L., Mauersberger, R., May, J., & Wilson, T. L. 2010, *A&A*, 523, A45
 Stolovy, S., et al. 2006, *Journal of Physics Conference Series*, 54, 176
 Urquhart, J. S., Hoare, M. G., Purcell, C. R., et al. 2010, *PASA*, 27, 321
 Walsh, A. J., Bertoldi, F., Burton, M. G., & Nikola, T. 2001, *MNRAS*, 326, 36
 Walsh, A. J., Breen, S. L., Britton, T., et al. 2011, *MNRAS*, 416, 1764
 Williams, J. P., de Geus, E. J., & Blitz, L. 1994, *ApJ*, 428, 693
 Yusef-Zadeh, F., et al. 2007, *IAU Symposium*, 242, 366
 Yusef-Zadeh, F., Hewitt, J. W., Arendt, R. G., et al. 2009, *ApJ*, 702, 178
 Yusef-Zadeh, F., Cotton, W., Viti, S., Wardle, M., & Royster, M. 2013a, *ApJ*, 764, L19
 Yusef-Zadeh, F., et al. 2013b, *JPhCh*, in press

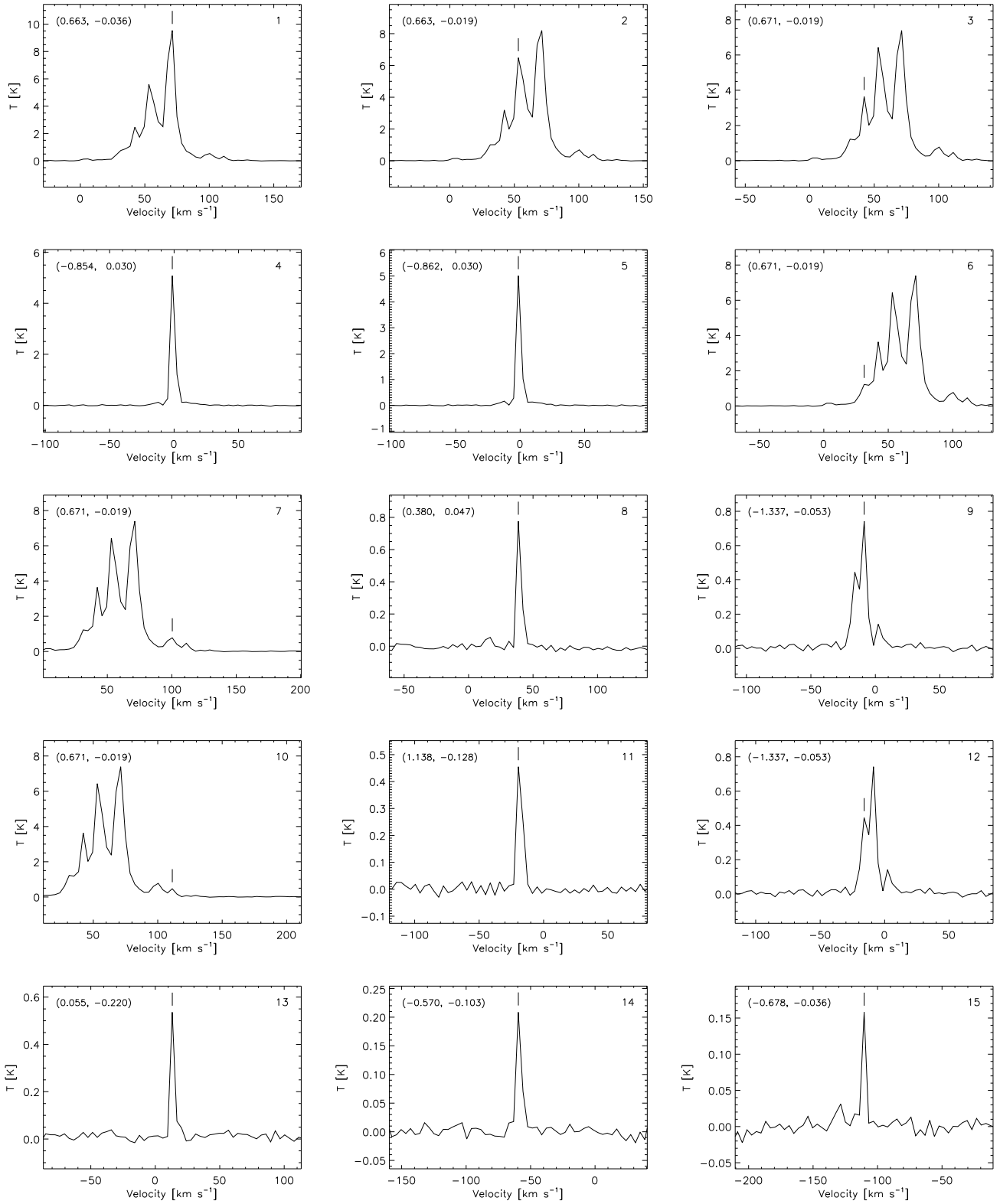


Fig. 10. Spectra of H₂O masers 1–15 detected in the survey region. The positions of the peak emission are printed on the spectra, and the numbers in the top-right of each plot correspond to the numbers in Table 3. The vertical line in each spectrum indicates the velocity of that maser.

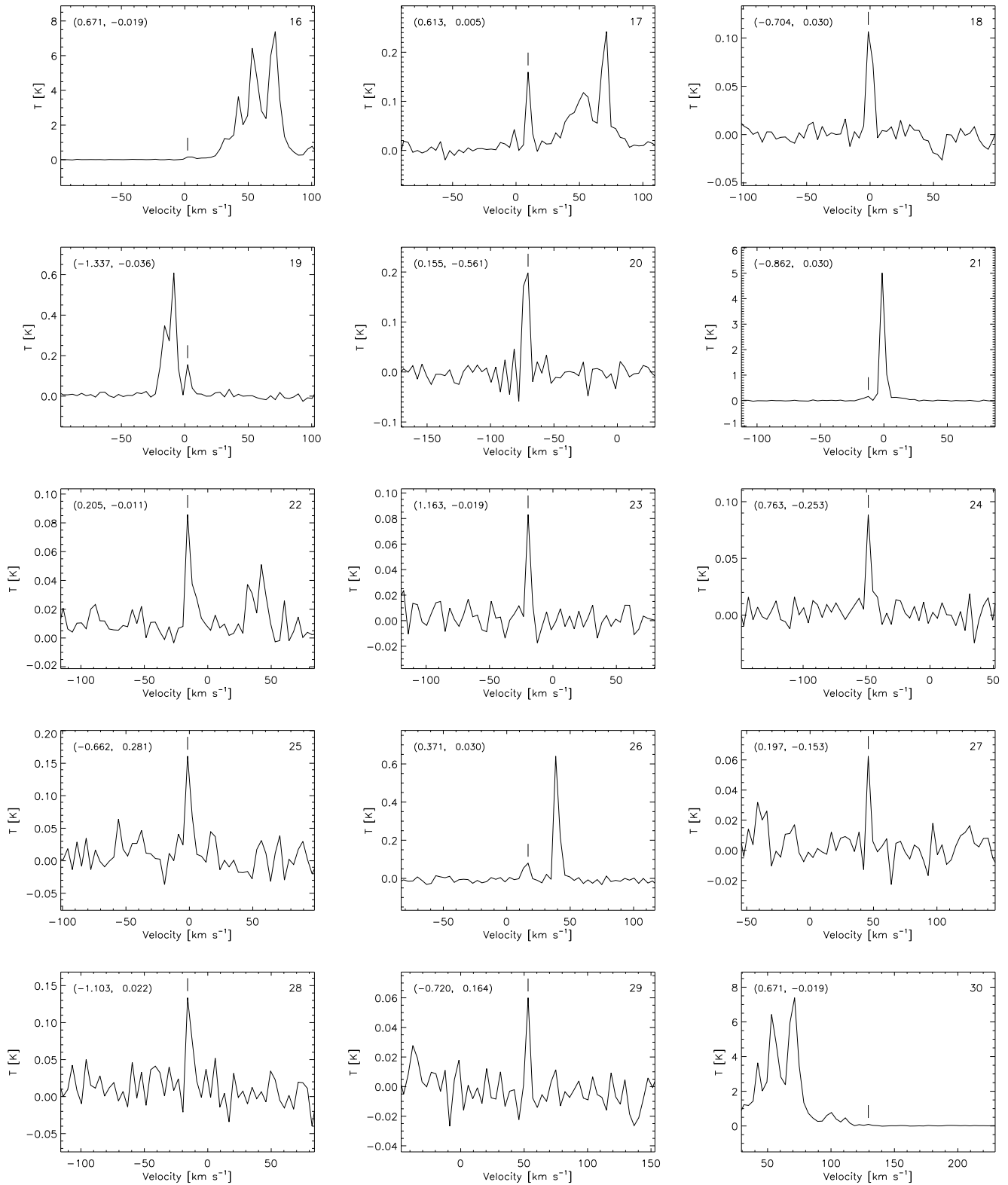


Figure 10, cont.

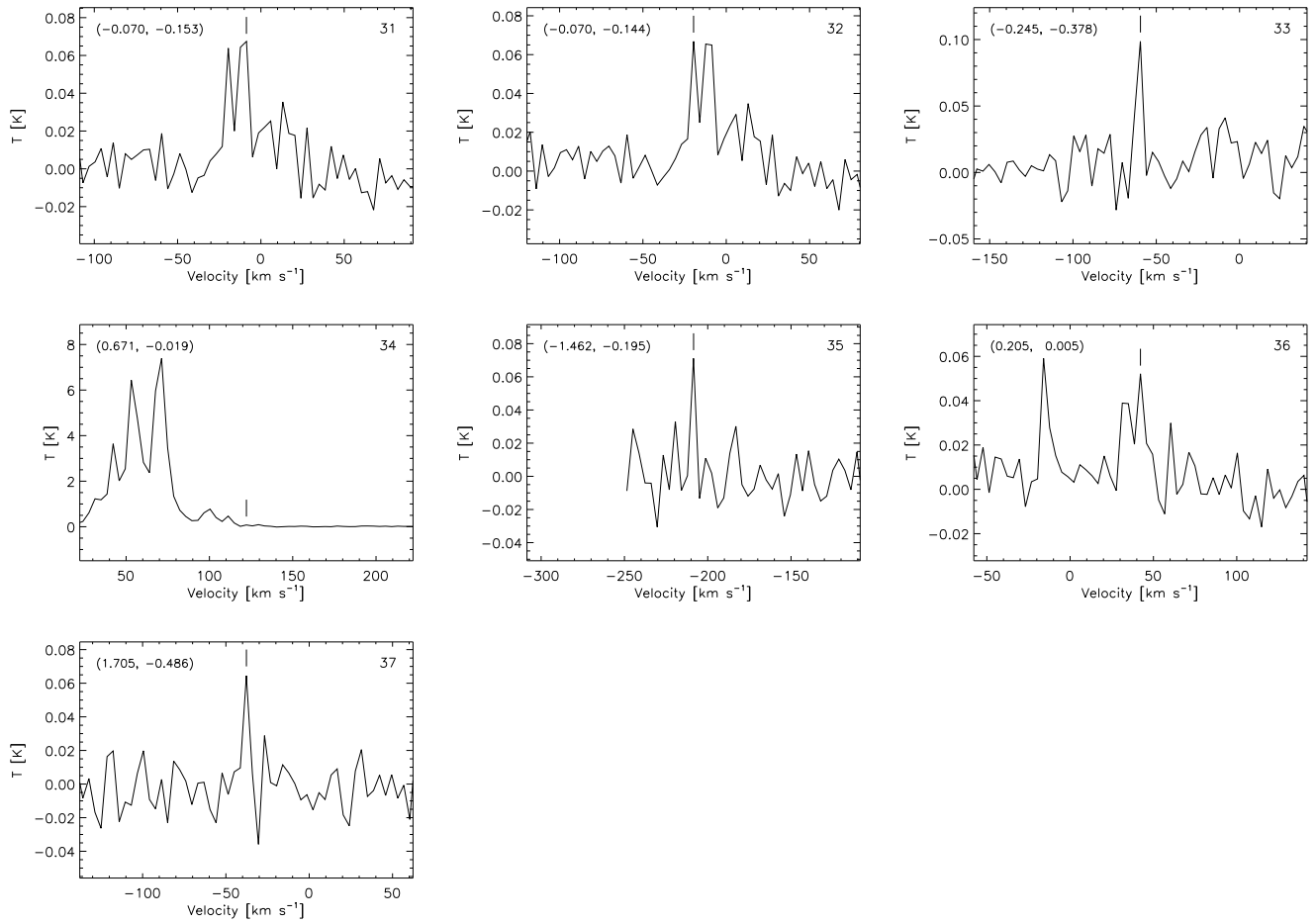


Figure 10, cont.

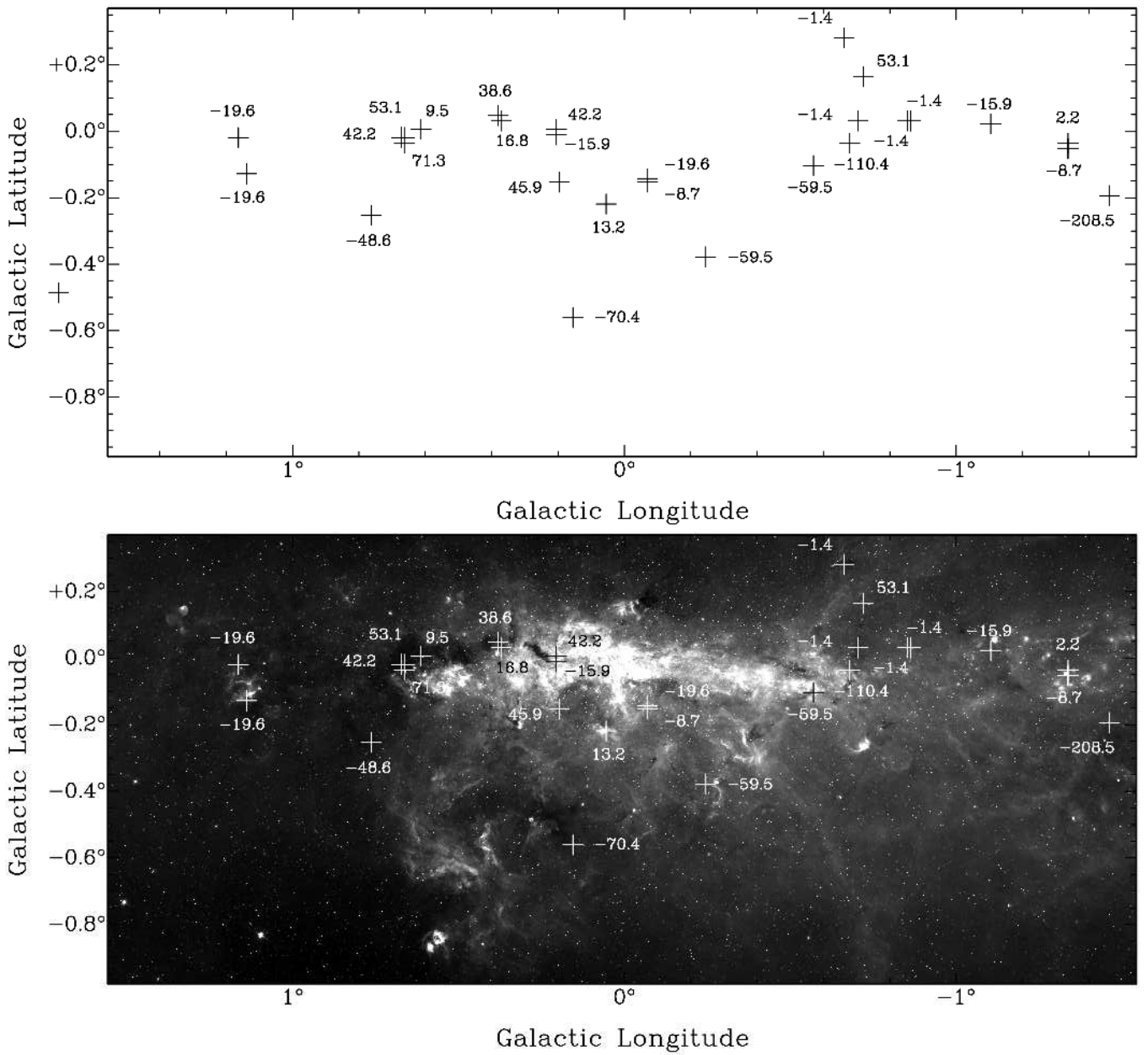


Fig. 12. *Top:* *Spitzer*/IRAC 8 μm image of the Galactic center region. Crosses (+) indicate the positions of the H₂O masers identified in the Mopra survey. Each maser is labelled with the velocity (in km s⁻¹) of the peak maser emission. *Bottom:* Same as the *top* figure, but with a blank background instead of the 8 μm image.

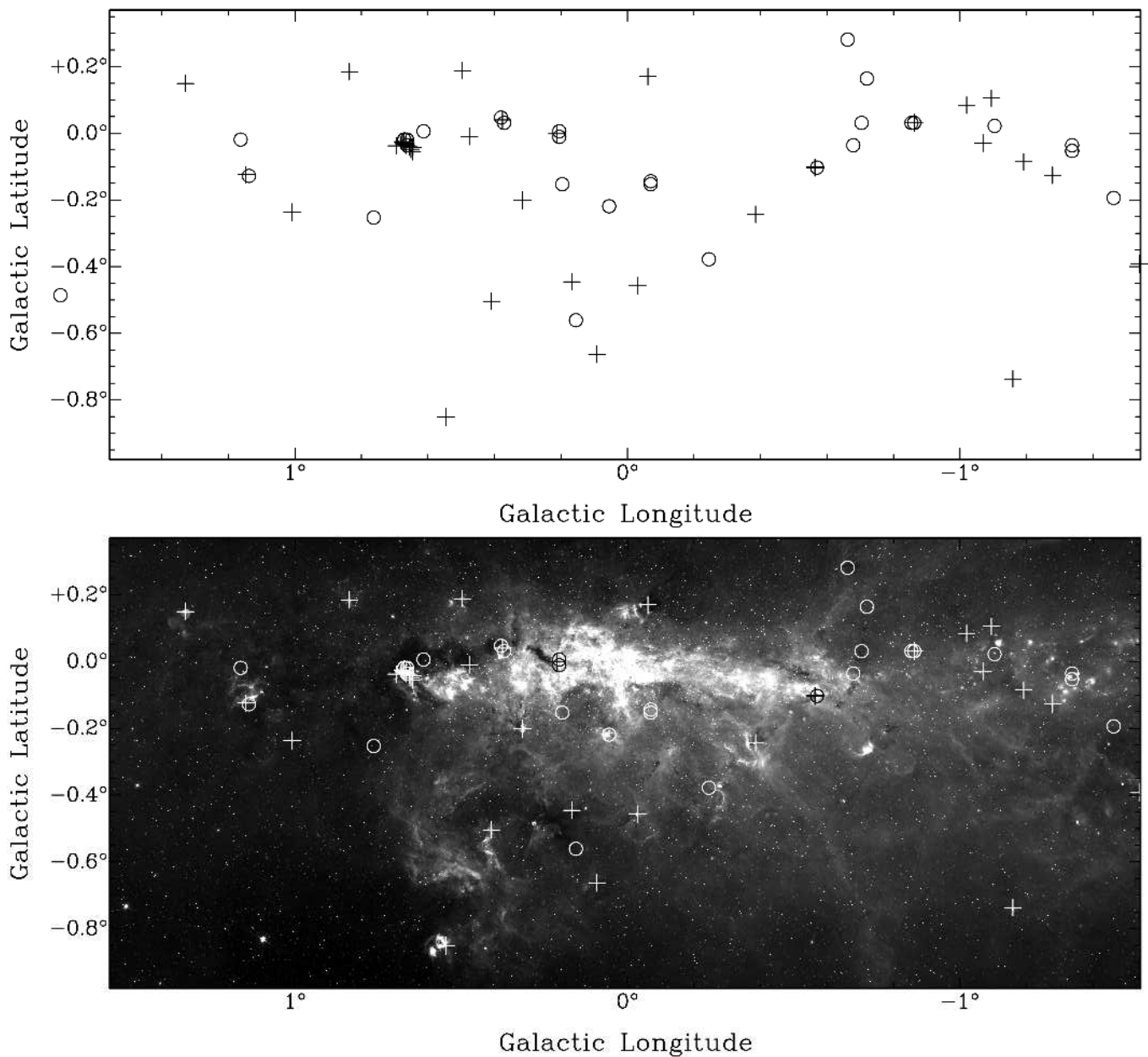


Fig. 14. *Top:* *Spitzer*/IRAC $8\ \mu\text{m}$ image of the Galactic center region showing both CH₃OH and H₂O masers. Circles indicate the positions of the H₂O masers identified in the Mopra survey. The size of the circle represents the FWHM of the Mopra beam at 22 GHz. Crosses (+) show the position of CH₃OH masers (the size of the crosses have no physical meaning). We consider a CH₃OH maser to be associated with a H₂O maser when it falls within the H₂O maser beam. For details on these associations, including their velocity information, see Table 4. *Bottom:* Same as the *top* figure, but with a blank background instead of the $8\ \mu\text{m}$ image.

Table 1. Association of Green Sources with CH₃OH Masers

Maser Name ^a	V_{peak}^a (km s ⁻¹)	R_{peak}		Value	R_{bg}	R_{cut}	R_{thresh}	N_{pix}	Green Source
		l^b	b^b						
G345.003-0.223	-23.1	345.0038	-0.2258	1.178	0.495	0.342	0.463	100	Y
G345.003-0.224	-26.2	345.0038	-0.2258	1.178	0.495	0.342	0.463	100	Y
G345.131-0.174	-28.9	345.1308	-0.1742	0.968	0.270	0.349	0.476	11	Y
G345.198-0.030	-0.5	345.1978	-0.0302	0.521	0.272	0.124	0.170	13	N
G345.205+0.317	-63.5	345.2048	0.3175	0.606	0.260	0.173	0.266	5	N
G345.407-0.952	-14.3	345.4065	-0.9518	0.429	0.170	0.130	0.167	4	N
G345.424-0.951	-13.2	345.4245	-0.9512	0.326	0.168	0.079	0.116	4	N
G345.441+0.205	0.9	345.4412	0.2048	0.695	0.276	0.209	0.312	7	N
G345.487+0.314	-22.6	345.4875	0.3152	0.513	0.240	0.137	0.184	52	N
G345.505+0.348	-17.8	345.5042	0.3465	1.029	0.351	0.339	0.437	87	Y
G345.576-0.225	-126.8	345.5762	-0.2255	0.683	0.292	0.196	0.291	13	Y
G345.807-0.044	-2	345.8068	-0.0442	0.828	0.287	0.271	0.416	7	N
G345.824+0.044	-10.3	345.8235	0.0432	0.912	0.268	0.322	0.435	10	Y
G345.949-0.268	-21.9	345.9495	-0.2678	0.671	0.294	0.189	0.295	12	Y
G345.985-0.020	-83.2	345.9852	-0.0202	1.191	0.249	0.471	0.605	13	Y
G346.036+0.048	-6.4	346.0362	0.0485	1.070	0.252	0.409	0.581	6	N
G346.231+0.119	-95	346.2325	0.1195	0.722	0.271	0.225	0.319	21	Y
G346.480+0.221	-18.9	346.4805	0.2212	1.162	0.307	0.427	0.620	13	Y
G346.481+0.132	-5.5	346.4815	0.1322	0.897	0.280	0.308	0.441	14	Y
G346.517+0.117	-1.7	346.5172	0.1175	0.402	0.223	0.090	0.129	3	N
G346.522+0.085	5.7	346.5225	0.0842	0.443	0.220	0.111	0.153	22	N
G347.230+0.016	-68.9	347.2302	0.0155	0.769	0.212	0.278	0.418	3	N
G347.583+0.213	-102.3	347.5835	0.2125	0.358	0.244	0.057	0.114	1	N
G347.628+0.149	-96.5	347.6278	0.1485	0.707	0.227	0.240	0.340	16	Y
G347.631+0.211	-91.9	347.6342	0.2082	0.343	0.232	0.056	0.101	2	N
G347.817+0.018	-24.1	347.8172	0.0178	0.926	0.264	0.331	0.449	8	N
G347.863+0.019	-34.7	347.8632	0.0185	0.632	0.234	0.199	0.291	9	Y
G347.902+0.052	-27.4	347.9042	0.0515	0.428	0.205	0.112	0.152	123	N
G348.027+0.106	-121.2	348.0268	0.1058	0.954	0.267	0.343	0.473	17	Y
G348.195+0.768	-0.8	348.1918	0.7665	1.076	0.332	0.372	0.744	1	N
G348.550-0.979	-10.6	348.5502	-0.9785	0.914	0.271	0.322	0.426	146	Y
G348.550-0.979n	-20	348.5502	-0.9785	0.914	0.271	0.322	0.426	146	Y
G348.579-0.920	-15.1	348.5785	-0.9198	1.062	0.440	0.311	0.411	148	Y
G348.654+0.244	16.9	348.6542	0.2445	0.747	0.275	0.236	0.355	11	Y
G348.723-0.078	11.5	348.7232	-0.0775	0.602	0.305	0.149	0.209	7	N
G348.703-1.043	-3.5	348.7032	-1.0422	0.309	0.177	0.066	0.085	36	N
G348.727-1.037	-7.4	348.7272	-1.0372	0.860	0.158	0.351	0.532	8	N
G348.884+0.096	-74.5	348.8845	0.0965	0.863	0.274	0.295	0.367	17	Y
G348.892-0.180	1.5	348.8918	-0.1795	1.140	0.282	0.429	0.630	5	N
G349.067-0.017	11.6	349.0672	-0.0168	0.593	0.262	0.166	0.241	12	Y
G349.092+0.105	-76.6	349.0915	0.1052	1.357	0.236	0.560	0.827	18	Y
G349.092+0.106	-81.5	349.0915	0.1052	1.357	0.236	0.560	0.827	18	Y
G349.151+0.021	14.6	349.1525	0.0222	0.697	0.268	0.215	0.279	7	N
G349.579-0.679	-25	349.5792	-0.6792	0.568	0.285	0.141	0.210	3	N
G349.799+0.108	-64.7	349.7985	0.1085	0.806	0.268	0.269	0.421	9	Y
G349.884+0.231	16.2	349.8832	0.2302	0.767	0.263	0.252	0.378	17	Y
G350.015+0.433	-30.3	350.0155	0.4332	0.615	0.241	0.187	0.261	16	Y
G350.104+0.084	-68.1	350.1048	0.0838	0.492	0.223	0.134	0.181	31	N
G350.105+0.083	-74.1	350.1048	0.0838	0.492	0.223	0.134	0.181	31	N
G350.116+0.084	-68	350.1168	0.0842	0.716	0.237	0.240	0.320	8	N
G350.116+0.220	4.2	350.1155	0.2205	0.997	0.279	0.359	0.541	4	N
G350.189+0.003	-62.4	350.1868	0.0022	0.711	0.268	0.221	0.343	4	N
G350.299+0.122	-62.1	350.2982	0.1198	0.700	0.231	0.234	0.334	31	Y
G350.340+0.141	-58.4	350.3402	0.1412	0.499	0.246	0.126	0.163	10	N
G350.344+0.116	-65.4	350.3438	0.1165	0.611	0.274	0.168	0.226	8	N
G350.356-0.068	-67.6	350.3562	-0.0678	0.874	0.263	0.306	0.431	19	Y
G350.470+0.029	-6.3	350.4702	0.0288	0.491	0.270	0.111	0.186	4	N
G350.520-0.350	-24.6	350.5195	-0.3492	1.017	0.269	0.374	0.547	14	Y
G350.686-0.491	-13.7	350.6855	-0.4905	1.349	0.312	0.519	0.749	10	Y

Table 1. continued.

Maser Name ^a	V_{peak}^a (km s ⁻¹)	R_{peak}		Value	R_{bg}	R_{cut}	R_{thresh}	N_{pix}	Green Source
		ℓ^b	b^b						
G350.776+0.138	38.7	350.7755	0.1382	0.826	0.255	0.286	0.380	4	N
G351.161+0.697	-5.2	351.1602	0.6968	0.853	0.392	0.231	0.321	517	Y
G351.242+0.670	2.5	351.2425	0.6708	0.377	0.194	0.092	0.136	54	N
G351.251+0.652	-7.1	351.2522	0.6515	0.620	0.166	0.227	0.290	61	Y
G351.382-0.181	-59.7	351.3822	-0.1808	0.807	0.277	0.265	0.407	10	Y
G351.417+0.645	-10.4	351.4168	0.6462	0.587	0.187	0.200	0.273	23	Y
G351.417+0.646	-11.1	351.4168	0.6462	0.587	0.187	0.200	0.273	23	Y
G351.445+0.660	-7.1	351.4442	0.6602	0.548	0.243	0.152	0.204	27	Y
G351.581-0.353	-94.2	351.5818	-0.3532	1.574	0.337	0.619	0.885	10	Y
G351.611+0.172	-43.7	351.6115	0.1698	0.284	0.195	0.044	0.075	309	N
G351.688+0.171	-36.1	351.6878	0.1708	0.726	0.258	0.234	0.343	13	Y
G351.775-0.536	1.3	351.7752	-0.5345	1.790	0.501	0.644	0.797	20	Y
G352.083+0.167	-66	352.0835	0.1672	0.615	0.259	0.178	0.259	13	Y
G352.111+0.176	-54.8	352.1108	0.1762	0.852	0.259	0.296	0.404	16	Y
G352.133-0.944	-7.7	352.1325	-0.9425	0.977	0.359	0.309	0.378	50	Y
G352.517-0.155	-51.2	352.5175	-0.1552	0.398	0.239	0.079	0.127	6	N
G352.525-0.158	-53	352.5248	-0.1582	0.854	0.238	0.308	0.483	7	N
G352.584-0.185	-85.7	352.5835	-0.1848	0.694	0.252	0.221	0.334	6	N
G352.604-0.225	-81.7	352.6042	-0.2252	0.829	0.284	0.272	0.368	14	Y
G352.855-0.201	-51.3	352.8548	-0.2005	0.616	0.231	0.193	0.295	4	N
G353.216-0.249	-22.9	353.2132	-0.2478	0.394	0.215	0.089	0.122	8	N
G353.273+0.641	-4.4	353.2725	0.6418	0.920	0.181	0.370	0.463	19	Y
G353.363-0.166	-79	353.3635	-0.1678	0.352	0.203	0.075	0.102	7	N
G353.370-0.091	-44.7	353.3705	-0.0905	0.462	0.251	0.105	0.154	16	N
G353.378+0.438	-15.7	353.3782	0.4375	0.419	0.252	0.084	0.115	4	N
G353.410-0.360	-20.3	353.4105	-0.3602	0.566	0.258	0.154	0.235	11	Y
G353.429-0.090	-61.8	353.4268	-0.0892	0.837	0.307	0.265	0.408	7	N
G353.464+0.562	-50.3	353.4635	0.5628	1.161	0.294	0.434	0.605	29	Y
G353.537-0.091	-56.6	353.5372	-0.0912	0.971	0.269	0.351	0.518	14	Y
G354.206-0.038	-37.1	354.2052	-0.0382	0.613	0.227	0.193	0.386	1	N
G354.308-0.110	18.8	354.3075	-0.1098	0.575	0.279	0.148	0.231	5	N
G354.496+0.083	27	354.4955	0.0825	0.390	0.238	0.076	0.098	14	N
G354.615+0.472	-24.4	354.6132	0.4718	0.619	0.284	0.168	0.228	37	Y
G354.701+0.299	102.8	354.6998	0.3002	0.975	0.323	0.326	0.537	4	N
G354.724+0.300	93.9	354.7232	0.3012	1.118	0.341	0.388	0.574	4	N
G355.184-0.419	-1.4 ^c	355.1825	-0.4188	1.557	0.403	0.577	0.720	15	Y
G355.343+0.148	5.8	355.3442	0.1475	0.485	0.270	0.107	0.157	14	N
G355.344+0.147	19.9	355.3442	0.1475	0.485	0.270	0.107	0.157	14	N
G355.346+0.149	10.5	355.3455	0.1492	0.510	0.273	0.118	0.184	4	N
G355.538-0.105	3.8	355.5382	-0.1045	0.603	0.272	0.165	0.245	29	Y
G355.545-0.103	-28.2	355.5452	-0.1035	0.566	0.267	0.150	0.210	20	Y
G355.642+0.398	-7.9	355.6418	0.3978	1.064	0.286	0.389	0.778	1	N
G355.666+0.374	-3.3	355.6665	0.3735	0.428	0.264	0.082	0.123	11	N
G356.054-0.095	16.7	356.0545	-0.0972	0.442	0.281	0.080	0.139	2	N
G356.662-0.263	-53.8	356.6612	-0.2628	1.188	0.356	0.416	0.570	9	Y
G357.558-0.321	-3.9	357.5575	-0.3215	0.776	0.328	0.224	0.307	8	N
G357.559-0.321	16.2	357.5575	-0.3215	0.776	0.328	0.224	0.307	8	N
G357.922-0.337	-4.6	357.9252	-0.3368	0.800	0.279	0.260	0.385	24	Y
G357.924-0.337	-2.1	357.9255	-0.3372	0.828	0.279	0.274	0.389	23	Y
G357.965-0.164	-8.6	357.9642	-0.1638	0.911	0.274	0.318	0.476	10	Y
G357.967-0.163	-3.1	357.9645	-0.1642	0.848	0.274	0.287	0.425	14	Y
G358.371-0.468	1.3	358.3712	-0.4685	0.799	0.231	0.284	0.425	20	Y
G358.386-0.483	-6	358.3868	-0.4812	0.585	0.281	0.152	0.226	178	Y
G358.460-0.391	1.3	358.4598	-0.3935	0.981	0.329	0.326	0.458	34	Y
G358.460-0.393	-7.3	358.4602	-0.3938	0.975	0.324	0.326	0.456	36	Y
G358.721-0.126	10.6	358.7215	-0.1262	0.917	0.316	0.301	0.410	6	N
G358.809-0.085	-56.2	358.8085	-0.0852	1.466	0.492	0.487	0.673	12	Y
G358.841-0.737	-20.7	358.8405	-0.7365	0.707	0.309	0.199	0.282	31	Y
G358.906+0.106	-18.1	358.9058	0.1045	0.530	0.363	0.083	0.107	4	N
G358.931-0.030	-15.9	358.9318	-0.0305	0.519	0.299	0.110	0.158	7	N

Table 1. continued.

Maser Name ^a	V_{peak}^a (km s ⁻¹)	R_{peak}			R_{bg}	R_{cut}	R_{thresh}	N_{pix}	Green Source
		l^b	b^b	Value					
G358.980+0.084	6.2	358.9798	0.0842	1.330	0.515	0.407	0.537	29	Y
G359.138+0.031	-3.9	359.1378	0.0325	0.503	0.306	0.099	0.142	23	N
G359.436-0.104	-47.8	359.4368	-0.1018	0.942	0.292	0.325	0.434	40	Y
G359.436-0.102	-53.3	359.4368	-0.1018	0.942	0.292	0.325	0.434	40	Y
G359.615-0.243	19.3	359.6125	-0.2415	1.154	0.328	0.413	0.559	9	Y
G359.938+0.170	-0.5	359.9382	0.1705	1.401	0.511	0.445	0.590	30	Y
G359.970-0.457	23	359.9692	-0.4588	0.735	0.263	0.236	0.313	42	Y
G0.092+0.663	23.8	0.0902	-0.6632	1.918	0.459	0.729	0.995	19	Y
G0.167-0.446	13.8	0.1672	-0.4438	1.330	0.362	0.484	0.690	14	Y
G0.212-0.001	49.5	0.2118	-0.0008	0.314	0.229	0.042	0.066	6	N
G0.315-0.201	19.4	0.3155	-0.2002	0.536	0.190	0.173	0.239	44	Y
G0.316-0.201	21.1	0.3155	-0.2002	0.536	0.190	0.173	0.239	44	Y
G0.376+0.040	37.1	0.3762	0.0402	1.114	0.342	0.386	0.550	14	Y
G0.409-0.504	25.4	0.4085	-0.5042	0.699	0.211	0.244	0.357	15	Y
G0.475-0.010	28.8	0.4748	-0.0098	0.374	0.317	0.029	0.048	4	N
G0.496+0.188	0.9	0.4965	0.1885	0.522	0.244	0.139	0.225	8	N
G0.546-0.852	11.8	0.5462	-0.8505	0.679	0.190	0.245	0.345	9	Y
G0.645-0.042	49.5	0.6438	-0.0405	0.847	0.293	0.277	0.366	6	N
G0.647-0.055	51 ^c	0.6462	-0.0552	0.510	0.282	0.114	0.183	2	N
G0.651-0.049	48.3	0.6528	-0.0498	0.430	0.285	0.073	0.108	3	N
G0.657-0.041	49.9 ^c	0.6578	-0.0415	0.856	0.291	0.282	0.385	19	Y
G0.665-0.036	60.4	0.6668	-0.0352	1.845	0.301	0.772	1.024	9	Y
G0.666-0.029	70.5	0.6662	-0.0288	0.483	0.283	0.100	0.145	4	N
G0.667-0.034	55 ^c	0.6668	-0.0352	1.845	0.301	0.772	1.024	9	Y
G0.672-0.031	58.2	0.6735	-0.0308	0.429	0.306	0.061	0.123	1	N
G0.673-0.029	66 ^c	0.6722	-0.0285	0.454	0.287	0.084	0.111	6	N
G0.677-0.025	73.3	0.6782	-0.0242	0.477	0.288	0.094	0.152	2	N
G0.695-0.038	68.6	0.6948	-0.0378	0.562	0.307	0.127	0.197	5	N
G0.836+0.184	3.5	0.8352	0.1848	0.314	0.245	0.035	0.070	1	N
G1.008-0.237	1.6	1.0085	-0.2378	0.450	0.266	0.092	0.135	19	N
G1.147-0.124	-15.3	1.1485	-0.1268	0.704	0.226	0.239	0.328	4	N
G1.329+0.150	-12.2	1.3285	0.1502	0.287	0.191	0.048	0.096	1	N
G1.719-0.088	-8.1	1.7188	-0.0878	1.203	0.374	0.414	0.543	6	N
G2.143+0.009	62.6	2.1448	0.0098	0.676	0.319	0.178	0.267	24	Y
G2.521-0.220	-6.1	2.5205	-0.2198	0.857	0.297	0.280	0.425	10	Y
G2.536+0.198	3.1	2.5358	0.1998	1.259	0.489	0.385	0.493	130	Y
G2.591-0.029	-8.3	2.5892	-0.0282	0.472	0.263	0.104	0.209	1	N
G2.615+0.134	94.1	2.6165	0.1345	0.380	0.264	0.058	0.084	6	N
G2.703+0.040	93.5	2.7062	0.0395	0.800	0.302	0.249	0.498	1	N
G3.253+0.018	2.2	3.2532	0.0185	0.727	0.306	0.211	0.346	5	N
G3.312-0.399	0.4	3.3118	-0.3965	1.649	0.413	0.618	0.939	10	Y
G3.442-0.348	-35.1	3.4418	-0.3482	2.928	0.388	1.270	1.946	4	N
G3.502-0.200	43.9	3.5008	-0.2008	1.081	0.333	0.374	0.517	6	N
G3.910+0.001	17.8	3.9102	0.0008	0.734	0.258	0.238	0.347	9	Y
G4.393+0.079	1.9	4.3935	0.0788	0.475	0.240	0.117	0.151	7	N
G4.434+0.129	-1	4.4342	0.1288	0.595	0.261	0.167	0.258	5	N
G4.569-0.079	9.5	4.5685	-0.0792	0.729	0.268	0.230	0.302	7	N
G4.586+0.028	26.1	4.5848	0.0252	0.609	0.280	0.164	0.329	1	N
G4.676+0.276	4.5	4.6752	0.2775	0.842	0.299	0.272	0.434	4	N
G4.866-0.171	5.4	4.8658	-0.1708	0.488	0.306	0.091	0.132	9	N
G5.618-0.082	-27.1	5.6188	-0.0812	1.113	0.294	0.410	0.523	15	Y
G5.630-0.294	10.5	5.6302	-0.2938	0.586	0.286	0.150	0.231	10	Y
G5.657+0.416	20	5.6555	0.4158	0.775	0.288	0.244	0.366	11	Y
G5.677-0.027	-11.7	5.6772	-0.0272	0.531	0.274	0.128	0.208	8	N
G5.885-0.393	6.7	5.8832	-0.3935	0.641	0.208	0.217	0.263	76	Y
G5.900-0.430	10.4	5.9002	-0.4318	0.224	0.153	0.035	0.049	5	N

Notes. ^(a) From C10. ^(b) Derived from IRAC data, which have a pixel size of 1.2". ^(c) For CH₃OH masers not detected in the C10 follow-up data, we use their survey cube data or the value they list from Houghton & Whiteoak (1995).

Table 4. Association of H₂O Masers with CH₃OH Masers

CH ₃ OH Masers			H ₂ O Masers				Angular	Green
Name	v_{low}^a (km s ⁻¹)	v_{high}^a (km s ⁻¹)	#	ℓ (°)	b (°)	v (km s ⁻¹)	Separation ($''$)	Source
G359.138+0.031	-7.0	1.0	4	-0.854	0.030	-1.4	33	N
			5	-0.862	0.030	-1.4	4	N
			21	-0.862	0.030	-12.3	4	N
G359.436-0.104	-53.0	-45.0	14	-0.570	-0.103	-59.5	23	Y
			G359.436-0.102	-58.0	-54.0	14	-0.570	-0.103
G0.212-0.001	41.0	50.5	22	0.205	-0.011	-15.9	45	N
			36	0.205	0.005	42.2	34	N
G0.376+0.040	35.0	40.0	8	0.380	0.047	38.6	30	Y
			26	0.371	0.030	16.8	38	Y
G0.645-0.042	46.0	53.0	1	0.663	-0.036	71.3	69	N
G0.651-0.049	46.0	49.0	1	0.663	-0.036	71.3	62	N
G0.657-0.041	48.0	56.0	1	0.663	-0.036	71.3	29	Y
G0.665-0.036	58.0	62.0	1	0.663	-0.036	71.3	6	Y
			2	0.663	-0.019	53.1	59	Y
			3	0.671	-0.019	42.2	64	Y
			6	0.671	-0.019	31.3	64	Y
			7	0.671	-0.019	100.4	64	Y
			10	0.671	-0.019	111.3	64	Y
			16	0.671	-0.019	2.2	64	Y
			30	0.671	-0.019	129.4	64	Y
			34	0.671	-0.019	122.2	64	Y
			G0.666-0.029	68.0	73.0	1	0.663	-0.036
2	0.663	-0.019				53.1	36	N
3	0.671	-0.019				42.2	38	N
6	0.671	-0.019				31.3	38	N
7	0.671	-0.019				100.4	38	N
10	0.671	-0.019				111.3	38	N
16	0.671	-0.019				2.2	38	N
30	0.671	-0.019				129.4	38	N
34	0.671	-0.019				122.2	38	N
G0.667-0.034	49.0	56.0				1	0.663	-0.036
			2	0.663	-0.019	53.1	53	Y
			3	0.671	-0.019	42.2	53	Y
			6	0.671	-0.019	31.3	53	Y
			7	0.671	-0.019	100.4	53	Y
			10	0.671	-0.019	111.3	53	Y
			16	0.671	-0.019	2.2	53	Y
			30	0.671	-0.019	129.4	53	Y
			34	0.671	-0.019	122.2	53	Y
			G0.672-0.031	55.0	59.0	1	0.663	-0.036
2	0.663	-0.019				53.1	54	N
3	0.671	-0.019				42.2	43	N
6	0.671	-0.019				31.3	43	N
7	0.671	-0.019				100.4	43	N
10	0.671	-0.019				111.3	43	N
16	0.671	-0.019				2.2	43	N
30	0.671	-0.019				129.4	43	N
34	0.671	-0.019				122.2	43	N
G0.673-0.029	65.5	66.5				1	0.663	-0.036
			2	0.663	-0.019	53.1	49	N
			3	0.671	-0.019	42.2	33	N
			6	0.671	-0.019	31.3	33	N
			7	0.671	-0.019	100.4	33	N
			10	0.671	-0.019	111.3	33	N
			16	0.671	-0.019	2.2	33	N
			30	0.671	-0.019	129.4	33	N
			34	0.671	-0.019	122.2	33	N
			G0.677-0.025	70.0	77.0	1	0.663	-0.036

Table 4. continued.

CH ₃ OH Masers			H ₂ O Masers			Angular Separation (")	Green Source	
Name	v_{low}^a (km s ⁻¹)	v_{high}^a (km s ⁻¹)	#	ℓ (°)	b (°)			v (km s ⁻¹)
			2	0.663	-0.019	53.1	54	N
			3	0.671	-0.019	42.2	28	N
			6	0.671	-0.019	31.3	28	N
			7	0.671	-0.019	100.4	28	N
			10	0.671	-0.019	111.3	28	N
			16	0.671	-0.019	2.2	28	N
			30	0.671	-0.019	129.4	28	N
			34	0.671	-0.019	122.2	28	N
G1.147-0.124	-20.5	-14.0	11	1.138	-0.128	-19.6	34	N

Notes. ^(a) For easier comparison with the H₂O masers, here we list the upper and lower bounds of the CH₃OH maser emission, as listed by C10.

Table 5. CH₃OH Masers not Associated with H₂O Masers

Name	ℓ ($^{\circ}$)	b ($^{\circ}$)	v_{low}^a (km s $^{-1}$)	v_{high}^a (km s $^{-1}$)	S_{peak} (Jy)	Green Source
G345.003-0.223	345.003	-0.223	-25.0	-20.1	236	Y
G345.003-0.224	345.003	-0.224	-33.0	-25.0	102	Y
G345.131-0.174	345.131	-0.174	-31.0	-28.0	3.1	Y
G345.198-0.030	345.198	-0.030	-4.0	1.0	2.53	N
G345.205+0.317	345.205	0.317	-64.1	-59.9	0.8	N
G345.407-0.952	345.407	-0.952	-15.5	-14.0	2	N
G345.424-0.951	345.424	-0.951	-21.0	-5.0	2.92	N
G345.441+0.205	345.441	0.205	-13.0	2.0	2.27	N
G345.487+0.314	345.487	0.314	-24.0	-21.5	2.5	N
G345.505+0.348	345.505	0.348	-23.1	-10.5	300	Y
G345.576-0.225	345.576	-0.225	-127.2	-122.0	0.64	Y
G345.807-0.044	345.807	-0.044	-3.0	-0.5	1	N
G345.824+0.044	345.824	0.044	-12.0	-9.0	3.17	Y
G345.949-0.268	345.949	-0.268	-22.5	-21.4	1.53	Y
G345.985-0.020	345.985	-0.020	-85.5	-81.7	5.7	Y
G346.036+0.048	346.036	0.048	-14.5	-3.9	8.99	N
G346.231+0.119	346.232	0.119	-96.6	-92.6	1.5	Y
G346.480+0.221	346.480	0.221	-21.0	-14.0	30.15	Y
G346.481+0.132	346.481	0.132	-11.6	-4.9	2.1	Y
G346.517+0.117	346.517	0.117	-3.0	1.0	0.3	N
G346.522+0.085	346.522	0.085	4.7	6.1	1.9	N
G347.230+0.016	347.230	0.016	-69.9	-68.0	0.86	N
G347.583+0.213	347.583	0.213	-103.8	-96.0	3.18	N
G347.628+0.149	347.628	0.149	-98.9	-95.0	19.2	Y
G347.631+0.211	347.631	0.211	-94.0	-89.0	5.81	N
G347.817+0.018	347.817	0.018	-26.0	-22.8	2.52	N
G347.863+0.019	347.863	0.019	-37.8	-28.0	6.38	Y
G347.902+0.052	347.902	0.052	-31.5	-27.0	5.37	N
G348.027+0.106	348.027	0.106	-122.8	-114.3	3.07	Y
G348.195+0.768	348.195	0.768	-2.8	-0.2	4.55	N
G348.550-0.979	348.550	-0.979	-19.0	-7.0	41.1	Y
G348.550-0.979n	348.550	-0.979	-23.0	-14.0	22.6	Y
G348.579-0.920	348.579	-0.920	-16.0	-14.0	0.32	Y
G348.654+0.244	348.654	0.244	16.5	17.5	0.82	Y
G348.723-0.078	348.723	-0.077	9.0	12.0	2.58	N
G348.703-1.043	348.704	-1.044	-17.5	-2.5	65	N
G348.727-1.037	348.727	-1.037	-12.0	-6.0	80.78	N
G348.884+0.096	348.885	0.097	-79.0	-73.0	12.18	Y
G348.892-0.180	348.892	-0.180	1.0	2.0	2.7	N
G349.067-0.017	349.067	-0.017	6.0	16.0	2.3	Y
G349.092+0.105	349.092	0.105	-78.0	-74.0	33.3	Y
G349.092+0.106	349.092	0.106	-83.0	-78.0	9.9	Y
G349.151+0.021	349.151	0.021	14.1	25.0	3.36	N
G349.579-0.679	349.579	-0.679	-26.0	-24.0	1.9	N
G349.799+0.108	349.798	0.108	-65.5	-57.4	3	Y
G349.884+0.231	349.884	0.231	13.5	17.5	6.96	Y
G350.015+0.433	350.015	0.433	-37.0	-29.0	7.2	Y
G350.104+0.084	350.104	0.084	-69.0	-67.5	9.9	N
G350.105+0.083	350.105	0.083	-76.0	-61.0	13.6	N
G350.116+0.084	350.116	0.084	-69.0	-67.0	10.3	N
G350.116+0.220	350.116	0.220	3.0	5.0	2.78	N
G350.189+0.003	350.189	0.003	-65.0	-62.0	1.07	N
G350.299+0.122	350.299	0.122	-70.0	-61.0	31.34	Y
G350.340+0.141	350.340	0.141	-60.0	-57.5	2.5	N
G350.344+0.116	350.344	0.116	-66.0	-55.0	19.9	N
G350.356-0.068	350.356	-0.068	-68.5	-66.0	1.44	Y
G350.470+0.029	350.470	0.029	-11.0	-5.5	1.44	N
G350.520-0.350	350.520	-0.349	-25.0	-22.0	1.67	Y
G350.686-0.491	350.686	-0.491	-15.0	-13.0	17.85	Y

Table 5. continued.

Name	ℓ ($^{\circ}$)	b ($^{\circ}$)	v_{low}^a (km s^{-1})	v_{high}^a (km s^{-1})	S_{peak} (Jy)	Green Source
G350.776+0.138	350.776	0.138	34.5	39.0	0.65	N
G351.161+0.697	351.161	0.697	-7.0	-2.0	17.02	Y
G351.242+0.670	351.242	0.670	2.0	3.0	0.74	N
G351.251+0.652	351.251	0.652	-7.5	-6.0	0.99	Y
G351.382-0.181	351.382	-0.181	-69.0	-58.0	19.66	Y
G351.417+0.645	351.417	0.645	-12.0	-6.0	3423	Y
G351.417+0.646	351.417	0.646	-12.0	-7.0	1840	Y
G351.445+0.660	351.445	0.660	-14.0	1.0	129	Y
G351.581-0.353	351.581	-0.353	-100.0	-88.0	47.5	Y
G351.611+0.172	351.611	0.172	-46.0	-31.5	4.2	N
G351.688+0.171	351.688	0.171	-47.5	-35.0	41.54	Y
G351.775-0.536	351.775	-0.536	-9.0	3.0	231	Y
G352.083+0.167	352.083	0.167	-68.2	-63.6	6.77	Y
G352.111+0.176	352.111	0.176	-61.0	-50.0	7.46	Y
G352.133-0.944	352.133	-0.944	-18.8	-5.6	16.32	Y
G352.517-0.155	352.517	-0.155	-52.0	-49.0	9.69	N
G352.525-0.158	352.525	-0.158	-62.0	-52.0	0.7	N
G352.584-0.185	352.584	-0.185	-92.6	-79.7	6.38	N
G352.604-0.225	352.604	-0.225	-85.0	-81.0	3.3	Y
G352.855-0.201	352.855	-0.200	-54.1	-50.1	1.29	N
G353.216-0.249	353.216	-0.249	-25.0	-15.0	5.14	N
G353.273+0.641	353.273	0.641	-7.0	-3.0	8.3	Y
G353.363-0.166	353.363	-0.166	-80.1	-78.3	2.79	N
G353.370-0.091	353.370	-0.091	-56.0	-43.4	1.35	N
G353.378+0.438	353.378	0.438	-16.5	-14.0	0.97	N
G353.410-0.360	353.410	-0.360	-23.0	-19.0	116	Y
G353.429-0.090	353.429	-0.090	-63.9	-45.0	13.39	N
G353.464+0.562	353.464	0.562	-52.7	-48.7	11.88	Y
G353.537-0.091	353.537	-0.091	-59.0	-54.0	2.51	Y
G354.206-0.038	354.205	-0.038	-37.5	-35.0	1.11	N
G354.308-0.110	354.308	-0.110	11.0	19.5	3.44	N
G354.496+0.083	354.495	0.083	17.5	27.5	8.41	N
G354.615+0.472	354.615	0.472	-27.0	-12.5	166	Y
G354.701+0.299	354.701	0.300	98.0	104.0	1.29	N
G354.724+0.300	354.724	0.300	91.0	95.0	12.58	N
G355.184-0.419	355.184	-0.419	-2.0	-0.5	1.35 ^b	Y
G355.343+0.148	355.343	0.148	4.0	7.0	1.24	N
G355.344+0.147	355.344	0.147	19.0	21.0	10.17	N
G355.346+0.149	355.346	0.149	9.0	12.5	7.39	N
G355.538-0.105	355.538	-0.105	-3.5	5.0	1.25	Y
G355.545-0.103	355.545	-0.103	-31.0	-27.5	1.22	Y
G355.642+0.398	355.642	0.398	-9.0	-6.9	1.44	N
G355.666+0.374	355.666	0.374	-4.5	0.6	2.47	N
G356.054-0.095	356.054	-0.095	15.6	17.7	0.52	N
G356.662-0.263	356.662	-0.263	-57.0	-44.0	8.38	Y
G357.558-0.321	357.558	-0.321	-5.5	0.0	2.16	N
G357.559-0.321	357.558	-0.321	15.0	18.0	2.01	N
G357.922-0.337	357.922	-0.337	-5.5	-4.0	0.97	Y
G357.924-0.337	357.924	-0.337	-4.5	3.0	2.34	Y
G357.965-0.164	357.965	-0.163	-9.0	3.0	2.74	Y
G357.967-0.163	357.967	-0.163	-6.0	0.0	47.5	Y
G358.371-0.468	358.371	-0.468	-1.0	13.0	44.01	Y
G358.386-0.483	358.386	-0.483	-7.0	-5.0	6.95	Y
G358.460-0.391	358.460	-0.391	-0.5	4.0	47.73	Y
G358.460-0.393	358.460	-0.393	-8.5	6.0	11.19	Y
G358.721-0.126	358.721	-0.126	8.8	13.9	2.99	N
G358.809-0.085	358.809	-0.085	-60.3	-50.5	6.86	Y
G358.841-0.737	358.841	-0.737	-30.0	-17.0	10.94	Y
G358.906+0.106	358.906	0.106	-20.5	-16.5	1.7	N
G358.931-0.030	358.931	-0.029	-22.0	-14.5	5.9	N

Table 5. continued.

Name	ℓ ($^{\circ}$)	b ($^{\circ}$)	v_{low}^a (km s^{-1})	v_{high}^a (km s^{-1})	S_{peak} (Jy)	Green Source
G358.980+0.084	358.980	0.084	5.0	7.0	<0.2	Y
G359.615-0.243	359.615	-0.243	14.0	27.0	38.62	Y
G359.938+0.170	359.938	0.170	-1.5	0.2	2.34	Y
G359.970-0.457	359.969	-0.457	20.0	24.1	2.39	Y
G0.092+0.663	0.092	-0.663	10.0	25.0	18.86	Y
G0.167-0.446	0.167	-0.446	9.5	17.0	1.33	Y
G0.315-0.201	0.315	-0.201	14.0	27.0	62.6	Y
G0.316-0.201	0.316	-0.201	20.0	22.0	0.58	Y
G0.409-0.504	0.409	-0.504	24.5	27.0	2.61	Y
G0.475-0.010	0.475	-0.009	23.0	31.0	3.14	N
G0.496+0.188	0.496	0.188	-12.0	2.0	24.51	N
G0.546-0.852	0.546	-0.851	8.0	20.0	61.92	Y
G0.647-0.055	0.647	-0.055	49.0	52.0	2.0 ^b	N
G0.695-0.038	0.695	-0.038	64.0	75.0	32.33	N
G0.836+0.184	0.836	0.185	2.0	5.0	6.64	N
G1.008-0.237	1.008	-0.237	1.0	7.0	13.57	N
G1.329+0.150	1.329	0.150	-13.5	-11.0	2.08	N
G1.719-0.088	1.719	-0.088	-9.0	-4.5	7.82	N
G2.143+0.009	2.143	0.009	54.0	65.0	7.08	Y
G2.521-0.220	2.521	-0.220	-7.5	5.0	1.02	Y
G2.536+0.198	2.536	0.198	2.0	20.5	29.4	Y
G2.591-0.029	2.591	-0.029	-9.5	-4.0	1.76	N
G2.615+0.134	2.615	0.134	93.5	104.0	1.22	N
G2.703+0.040	2.703	0.040	91.5	98.0	8.97	N
G3.253+0.018	3.253	0.019	-1.5	3.5	3.54	N
G3.312-0.399	3.312	-0.399	0.0	10.0	1.17	Y
G3.442-0.348	3.442	-0.348	-35.5	-34.5	1.06	N
G3.502-0.200	3.502	-0.200	43.0	45.5	1.57	N
G3.910+0.001	3.910	0.001	15.0	24.5	5.04	Y
G4.393+0.079	4.393	0.079	0.0	9.0	6.74	N
G4.434+0.129	4.434	0.129	-1.5	8.0	3.29	N
G4.569-0.079	4.569	-0.079	9.0	10.0	0.44	N
G4.586+0.028	4.586	0.028	15.0	27.0	1.16	N
G4.676+0.276	4.676	0.276	-5.5	6.0	2.06	N
G4.866-0.171	4.866	-0.171	5.0	6.0	0.56	N
G5.618-0.082	5.618	-0.082	-28.0	-18.5	3.37	Y
G5.630-0.294	5.630	-0.294	9.0	22.0	1.28	Y
G5.657+0.416	5.657	0.416	13.0	22.0	1.75	Y
G5.677-0.027	5.677	-0.027	-14.5	-11.0	0.79	N
G5.885-0.393	5.885	-0.393	6.0	7.5	0.48	Y
G5.900-0.430	5.900	-0.429	0.0	10.6	6.2	N

Notes. ^(a) For easier comparison with the H₂O masers, here we list the upper and lower bounds of the CH₃OH maser emission, as listed by C10.

^(b) For CH₃OH masers not detected in the C10 follow-up data, we use their survey cube data or the value they list from Houghton & Whiteoak (1995).